International Journal of Engineering Science 226 (2026) 104576

Contents lists available at ScienceDirect

International Journal of Engineering Science

journal homepage: www.elsevier.com/locate/ijengsci

Full length article

A FEM-based iterative method for Mindlin integral nonlocal plates

Andrea Caporale [a,b,*], Marzia Sara Vaccaro [c], Raffaele Barretta [c], Raimondo Luciano [d]

[a] Department of Civil and Mechanical Engineering, University of Cassino and Southern Lazio, via G. Di Biasio 43, 03043 Cassino, Italy
[b] European University of Technology, European Union
[c] Department of Structures for Engineering and Architecture, University of Naples Federico II, Via Claudio 21, 80125 Naples, Italy
[d] Department of Engineering, University of Naples Parthenope, via Amm. F. Acton 38, 80133 Naples, Italy

ARTICLE INFO

Keywords:
Nanoplates
Nonlocal continuum mechanics
Iterative methods
FEM

ABSTRACT

Shear-deformable nanoplates are investigated within a constitutive framework combining local and stress-driven nonlocal elastic phases. Size effects are incorporated through integral convolutions of the stress resultants. The resulting governing equations are solved by a FEM-based iterative procedure, consisting of a sequence of linear boundary-value problems terminated upon satisfaction of a convergence criterion. By setting the local phase to zero, the proposed formulation reduces to the purely nonlocal model, which has been widely and successfully employed in nonlocal analysis of one-dimensional nanostructures, such as nanobeams. Although iterative solution schemes are known to be effective for purely nonlocal one-dimensional problems, the present study shows that convergence issues arise when such approaches are applied to purely nonlocal two-dimensional structures. By contrast, the proposed mixed local–nonlocal model exhibits robust numerical behavior, ensuring rapid, stable convergence of the iterative scheme. Using the mixed model, convergence is achieved to arbitrary accuracy, up to machine precision, for both moderately thick and thin nanostructured elements (plates and beams) with arbitrary geometry, boundary conditions, loading, and nonlocal convolution kernels. This robustness across structurally and physically diverse nanostructures highlights the generality of the proposed approach and supports its applicability to a broad class of nanoengineered systems. Representative numerical examples are provided to illustrate and support these findings.

1. Introduction

Nanoplates (Barretta, Faghidian et al., 2019; Farajpour et al., 2020; Grekov & Bochkarev, 2024) are fundamental components in nano- and micro-scale engineering applications, including nanoelectromechanical systems (NEMS) (Xiao et al., 2025; Xie et al., 2025; Zhang et al., 2024; Zhou et al., 2025), flexible electronics (Batool et al., 2025; Liu et al., 2026), layered structures (Sadeghian et al., 2024; Wang et al., 2025), and metamaterials (Karami & Ghayesh, 2025). At these length scales, classical continuum theories are often unable to capture experimentally observed size-dependent effects (Fleck & Hutchinson, 1997; Lam et al., 2003), such as stiffness enhancement, scale-dependent bending response, and anomalous deformation patterns. The emergence

* Corresponding author at: Department of Civil and Mechanical Engineering, University of Cassino and Southern Lazio, via G. Di Biasio 43, 03043 Cassino, Italy.
E-mail address: a.caporale@unicas.it (A. Caporale).

https://doi.org/10.1016/j.ijengsci.2026.104576
Received 14 February 2026; Received in revised form 11 May 2026; Accepted 12 May 2026
Available online 27 May 2026

of innovative materials and architectures necessitates the development of advanced methodologies capable of characterizing non-classical structural responses (Barchiesi et al., 2021; Behnam-Rasouli et al., 2024; Izadi et al., 2024; Nguyen et al., 2025; Penna & Lovisi, 2025; Rezaei et al., 2025).

In the generalized continuum models (Maugin, 2017), incorporating intrinsic material length scales, nonlocal elasticity (Eringen, 1972, 1992; Nazmul & Devnath, 2021; Numanoğlu et al., 2022; Peddieson et al., 2003; Wang & Liew, 2007), and strain-gradient theories (Akgöz & Civalek, 2011, 2022; Lam et al., 2003) play a central role.

Nonlocal continuum theories account for long-range interatomic interactions by relating stresses or strains at a material point to the state of a surrounding region. The pioneering works of Eringen (1972) and Kröner (1967) established the theoretical foundations of nonlocal elasticity, which has since been extensively applied to beams, plates, and shells at the nanoscale. However, application of Eringen's nonlocal elasticity to structural mechanics problems has revealed several paradoxical and counterintuitive results, as first reported by Peddieson et al. (2003). In particular, nonlocal differential models have been shown to exhibit ill-posedness and nonphysical responses in some nanobeam applications. To overcome these limitations, Challamel and Wang (2008) introduced an elastic model based on combining the local and the nonlocal curvatures in the constitutive elastic relation of cantilever beams. Romano et al. (2017) elucidated the origin of these paradoxes by demonstrating that the field variables cannot, in general, satisfy the constitutive boundary conditions, which must be intrinsically coupled with the governing differential equations. Furthermore, they showed that introducing a convex combination of local and nonlocal phases restores well-posedness of the problem (see also Barretta et al. (2024, 2023), Fernández-Sáez and Zaera (2017) and Khaniki (2019)).

An alternative and conceptually distinct strategy was developed by Romano and Barretta (2017), who introduced a stress-driven nonlocal formulation. In this framework, the stress field is treated as the primary input, in contrast to strain-driven approaches — such as Eringen's differential nonlocal model — where elastic strain is the input. The stress-driven model has been shown to restore well-posedness (Romano et al., 2018) and eliminate nonlocal paradoxes, and has been successfully applied to the solution of a wide class of nonlocal structural problems (Alotta et al., 2025; Barretta et al., 2022; Caporale et al., 2022, 2023; Darban et al., 2022; Jafarinezhad et al., 2023; Lovisi et al., 2024).

In parallel with these theoretical and numerical developments, nanocoatings have attracted increasing attention due to their ability to markedly enhance the mechanical and functional performance of engineering surfaces. Nanocoatings — defined as a thin layer of thickness about <100 nm, deposited on the substrate for improving some property or for imparting new functionality — exhibit size-dependent properties arising from grain refinement, interface density, and nanoscale confinement effects (Meyers et al., 2006; Voevodin & Zabinski, 2005). Ceramic, metallic, and nanocomposite nanocoatings are widely employed to improve hardness, wear resistance, corrosion protection, and thermal stability in applications ranging from cutting tools and energy systems to biomedical implants and microelectronics (Farooq et al., 2022; Nguyen-Tri et al., 2018). The mechanical response of nanocoatings is strongly affected by substrate interaction and thickness effects, which are commonly investigated through nanoindentation experiments and interpreted using advanced continuum models that incorporate nonlocal or gradient effects (Li & Vlassak, 2009; Saha & Nix, 2002). Consequently, refined plate and shell theories that account for size effects are increasingly relevant for the predictive modeling of coated nanosystems, layered nano-architectures, and nanocoatings.

2. Motivation and outline

For plate-like nanostructures, adoption of shear deformation theories is essential, especially for thick/moderately thick nanoplates and layered configurations where transverse shear effects are non-negligible. Nonlocal elasticity models have been applied to both classical and first-order shear deformation plate theories (Reddy, 2010). Several subsequent studies have further investigated this topic (Ansari & Gholami, 2016; Lu et al., 2018; Saini & Pradyumna, 2023; Shaat, 2015). Nonlocal Mindlin (first-order shear deformation) plate theory has been adopted in various numerical methodologies, e.g. Li et al. (2025) developed a hybrid finite element method and Hu et al. (2020) presented a new state-based PeriDynamic model of a composite laminate. Piezoelectric nanoplates exploiting Mindlin plate theories have been modeled by He et al. (2024). Size-dependent Kirchhoff and Mindlin plate models have been developed by Lu et al. (2018). Postbuckling of composite annular Mindlin microplates has been addressed by Ke et al. (2014). Nonlocal mechanics of Mindlin plates made of polymer networks has been investigated by Xu and Wang (2025). Additionally, it has been shown that classical and first-order shear plate theories are special cases of a unified plate theory that also encompasses refined and higher-order shear-deformation models (Lu et al., 2019). Based on molecular dynamics (MD) simulation results for wave propagation, Yang et al. (2026) demonstrated that nonlocal plate models incorporating Mindlin, second-order, and third-order shear deformation theories are suitable for analyzing wave propagation, whereas the classical Kirchhoff plate theory is not appropriate for such analyses.

In this context, the present work develops a finite element formulation for the elastostatic analysis of shear-deformable Mindlin nanoplates. A two-phase local–nonlocal elasticity model is adopted, in which size-dependent effects are captured through a stress-driven nonlocal phase defined by an integral convolution operator. The resulting problem is governed by a system of integro-partial differential equations, whose analytical treatment and numerical solution are generally challenging, thereby motivating the development of robust and efficient computational strategies.

Many authors (Li et al., 2021; Nateghi-Babagi et al., 2025) recognize that solving nonlocal problems in their original integral form is generally very complex. Adopting a differential formulation in place of the integral one appears to be an alternative approach for solving the nonlocal problems. In some cases, the differential form cannot correctly capture nonlocal behavior, and the integral form should be used to avoid inconsistent results, as noted in Ansari et al. (2018), one of the few studies showing the differential form's inconsistencies in two-dimensional problems. Specifically, imposing the free boundary condition at the edges of the nanoplate

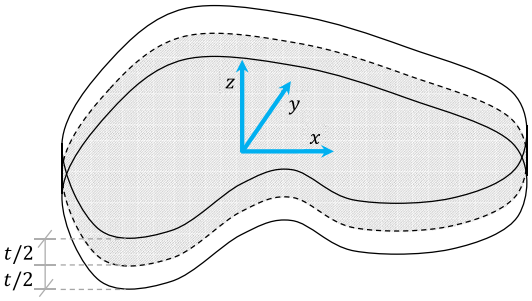

Fig. 1. Geometry of the plate model.

(e.g., a cantilever nanoplate) yields inconsistent results for the differential model of the nonlocal theory. Furthermore, Ansari et al. (2018) claim that the integral formulation of Eringen's nonlocal model can appropriately resolve this paradox, also allowing the adoption of arbitrary kernel functions. Integral formulations have also been used in one-dimensional problems to eliminate the well-known inconsistencies of classical differential nonlocal models and to obtain paradox-free results (Fallahzadeh Rastehkenari et al., 2026), without the need to adopt the differential transformation and its additional compelling constitutive boundary conditions. The importance of the integral nonlocal approach is well highlighted by Ding and Semperlotti (2024), who review existing finite element methods for integral nonlocal elasticity: they observe that, although these studies have achieved notable advancements, the application of these approaches is still limited to nonlocal problems with 1D kernels and does not extend to more generalized high-dimensional nonlocal problems with irregular geometries.

For specific classes of attenuation kernels and under particular geometric assumptions, the integro-differential formulation can be equivalently recast into a system of differential equations supplemented by constitutive boundary conditions. This equivalence has been rigorously established for axisymmetric nanoplates and related configurations in several recent contributions (Barretta, Faghidian et al., 2019; Jafarinezhad et al., 2023, 2024; Vaccaro & Sedighi, 2023). Following a similar rationale, Farajpour et al. (2020) derived a differential formulation for rectangular nanoplates by adopting a suitable choice of the nonlocal kernel.

An alternative and numerically attractive approach to nonlocal elasticity problems was introduced by Romano et al. (2019), who proposed an iterative solution strategy that avoids the explicit introduction of constitutive boundary conditions arising in differential nonlocal formulations. Within this framework, the nonlocal response is recovered by solving a sequence of standard local elastostatic problems, significantly simplifying the numerical implementation. This methodology was successfully applied to one-dimensional structures, such as Bernoulli–Euler nanobeams, within a stress-driven purely nonlocal formulation (Romano et al., 2019).

In the present study, iterative methods are applied, for the first time, to shear-deformable nanoplates. Following the approach by Romano et al. (2019), an iterative scheme is initially formulated for stress-driven purely nonlocal nanoplates. However, the emergence of convergence difficulties motivates the investigation of alternative models to the purely nonlocal one. In this regard, the two-phase local–nonlocal formulation exhibits markedly improved numerical performance and is therefore adopted as the final framework for the analysis of shear-deformable nanoplates. Particular attention is devoted to the convergence properties of the iterative scheme, the influence of nonlocal parameters, and the role of mesh refinement. The proposed approach provides an accurate, computationally efficient framework for analyzing nanoscale plates and offers valuable insights for modeling and designing advanced nanostructured and coated systems.

The proposed iterative method, based on solving a sequence of local finite element problems, exhibits notable convergence properties stemming from the well-established local FEM. The convergence of finite element methods involving nonlocal operators is more complicated to analyze than that of the local FEM (used in the next sections) and is affected by many factors (Ding & Semperlotti, 2024). Shaat (2015) has also used an iterative method for Kirchhoff plates, based on a local prediction/nonlocal correction procedure, achieving good convergence in a few iterations. Romano et al. (2019) have expressed some concerns regarding the strain-driven approach used in Shaat (2015). Shaat (2015) determines an analytical solution at each iteration, therefore, requiring the adoption of specific geometries, e.g., rectangular plates. The FEM-based method developed in the next sections offers the advantages of numerical methods, i.e., the ability to handle generalized integral kernel functions and non-regular (non-rectangular) domains (Ding & Semperlotti, 2024), as well as the convergence properties of local FEM.

The paper is organized as follows. In Section 3, the Mindlin plate theory is briefly recalled, and the two-phase local–nonlocal model is formulated for shear-deformable nanoplates. Section 4 introduces the proposed iterative solution strategy, whereby the nonlocal response is obtained through the repeated solution of local problems. The finite element discretization and numerical integration procedures are described in Section 5. Representative numerical examples and parametric studies are presented in Section 6, and concluding remarks are drawn in Section 7.

3. Mindlin theory for local plates and nonlocal nanoplates

The proposed method can be applied to nanoplates of arbitrary geometry, such as the one shown in Fig. 1. The plate thickness is denoted by t, and the z-axis is taken along the thickness direction. The mid-plane of the plate is equidistant from the plate surfaces perpendicular to the z-axis, and is colored gray in Fig. 1.

Table 1
Nomenclature for Sections 3, 4, and 6.

Symbol	Meaning
α	Parameter governing the two-phase local–nonlocal mixture
$\mathbb{B}_\mathrm{b}$, $\mathbb{B}_\mathrm{s}$	Generalized strain–displacement matrices, $\boldsymbol{\chi} = \mathbb{B}_\mathrm{b}\boldsymbol{u}$, $\boldsymbol{\gamma}_\mathrm{s} = \mathbb{B}_\mathrm{s}\boldsymbol{u}$
β	Model parameter, $\beta^{-1} = 5\,(1-\nu)\,L^2/t^2$
$\boldsymbol{C}_\mathrm{b}$, $\boldsymbol{C}_\mathrm{s}$	Material stiffness matrices, $\boldsymbol{\sigma}_\mathrm{b} = \boldsymbol{C}_\mathrm{b}\,\boldsymbol{\varepsilon}_\mathrm{b}^\mathrm{lc}$, $\boldsymbol{\tau}_\mathrm{s} = \boldsymbol{C}_\mathrm{s}\,\boldsymbol{\gamma}_\mathrm{s}^\mathrm{lc}$
$\boldsymbol{\chi}$, $\boldsymbol{\gamma}_\mathrm{s}$	Total generalized strains, $\boldsymbol{\chi} = \boldsymbol{\chi}^\mathrm{el} + \boldsymbol{\chi}^\mathrm{in}$, $\boldsymbol{\gamma}_\mathrm{s} = \boldsymbol{\gamma}_\mathrm{s}^\mathrm{el} + \boldsymbol{\gamma}_\mathrm{s}^\mathrm{in}$
$\boldsymbol{\chi}^\mathrm{el}$, $\boldsymbol{\gamma}_\mathrm{s}^\mathrm{el}$	Elastic generalized strains
$\boldsymbol{\chi}^\mathrm{in}$, $\boldsymbol{\gamma}_\mathrm{s}^\mathrm{in}$	Inelastic generalized strains
$\boldsymbol{\chi}^\mathrm{lc}$, $\boldsymbol{\gamma}_\mathrm{s}^\mathrm{lc}$	Local elastic generalized strains, $\boldsymbol{\chi}^\mathrm{lc} = \boldsymbol{D}_\mathrm{b}^{-1}\boldsymbol{M}$, $\boldsymbol{\gamma}_\mathrm{s}^\mathrm{lc} = \boldsymbol{D}_\mathrm{s}^{-1}\boldsymbol{Q}$
$\boldsymbol{\chi}^\mathrm{mix}$, $\boldsymbol{\gamma}_\mathrm{s}^\mathrm{mix}$	Elastic generalized strains of the mixture, e.g. $\boldsymbol{\chi}^\mathrm{mix} = \alpha\boldsymbol{\chi}^\mathrm{lc} + (1-\alpha)\,\boldsymbol{\chi}^\mathrm{nl}$
$\boldsymbol{\chi}^\mathrm{nl}$, $\boldsymbol{\gamma}_\mathrm{s}^\mathrm{nl}$	Nonlocal elastic generalized strains, $\boldsymbol{\chi}^\mathrm{nl} = \psi * \boldsymbol{\chi}^\mathrm{lc}$, $\boldsymbol{\gamma}_\mathrm{s}^\mathrm{nl} = \psi * \boldsymbol{\gamma}_\mathrm{s}^\mathrm{lc}$
$\boldsymbol{D}_\mathrm{b}$	Moment–curvature stiffness matrix, $\boldsymbol{D}_\mathrm{b} = t^3\,\boldsymbol{C}_\mathrm{b}/12$
$\boldsymbol{D}_\mathrm{s}$	Shear force-strain stiffness matrix, $\boldsymbol{D}_\mathrm{s} = t\,\boldsymbol{C}_\mathrm{s}$
D	Scalar stiffness, $D = \frac{Et^3}{12(1-\nu^2)}$
E, G	Young's modulus and shear modulus, respectively
$\boldsymbol{\varepsilon}_\mathrm{b}$, $\boldsymbol{\gamma}_\mathrm{s}$	Strain vectors
L	Maximum length of the plate, $L = L_x \geq L_y$
L_c	Length-scale parameter
L_x, L_y	Lengths of the plate along the x- and y-axis, respectively
λ_c	Dimensionless length-scale parameter, $\lambda_c = L_c/L_x$
$\boldsymbol{M}$, $\boldsymbol{Q}$	Moment and shear force vectors, respectively
M_x, M_y	Bending moments
M_{xy}	Twisting moment
n_x, n_y	Number of finite elements along the x- and y-axes, respectively
ν	Poisson's Ratio
P_lc	Local elastostatic operator
ψ	Kernel function
q	Transverse distributed load
$\bar{q}$	Dimensionless transverse load, $\bar{q} = qL^3/D$
$\boldsymbol{r}^{(i)}$	Relative residual at the ith iteration
$\boldsymbol{\sigma}_\mathrm{b}$, $\boldsymbol{\tau}_\mathrm{s}$	Stress vectors
t	Thickness of the plate
ϕ_x, ϕ_y	Rotations around the y- and x-axes, respectively
u, v	Displacements along the x- and y-axes, respectively
w	Transverse displacement (along the z-axis)
$\bar{w}$	Dimensionless transverse displacement, $\bar{w} = w/L$
$w^{(i)}$	Transverse displacement at the ith iteration
$w^{(0)}$	Transverse displacement at iteration 0, i.e. the local displacement
w_max	Maximum transverse displacement
$\bar{w}^{(i)}, \bar{w}^{(0)}, \bar{w}_\mathrm{max}$	Dimensionless form of displacements $w^{(i)}, w^{(0)}, w_\mathrm{max}$, respectively
x, y, z	Cartesian coordinates
$\bar{x}, \bar{y}$	Dimensionless Cartesian coordinates, $\bar{x} = x/L_x$, $\bar{y} = y/L_y$

The displacements along the x-, y-, and z-axes are denoted by u, v, and w, respectively. The rotations around the x- and y-axes are named ϕ_y and ϕ_x, respectively, and are such that positive values of these rotations produce negative components u and v for $z > 0$. Next, the equations of the Mindlin plates are recalled. Then, the stress-driven integral form of nonlocal elasticity is applied to Mindlin nanoplates (see Tables 1 and 2 for definitions).

3.1. Kinematics

The geometrically linearized Mindlin theory of plates gives the following expressions for the displacements u and v parallel to the mid-plane

$$u = -z\,\phi_x, \quad v = -z\,\phi_y. \tag{1}$$

The non-zero components of the total tangent deformation are collected in two different vectors: $\boldsymbol{\varepsilon}_\mathrm{b}$ responsible for bending and twisting deformations, and $\boldsymbol{\gamma}_\mathrm{s}$ representing the transverse shear strains, i.e.

$$\boldsymbol{\varepsilon}_\mathrm{b} = \begin{Bmatrix} \varepsilon_x \\ \varepsilon_y \\ \gamma_{xy} \end{Bmatrix} = \begin{Bmatrix} \frac{\partial u}{\partial x} \\ \frac{\partial v}{\partial y} \\ \frac{\partial u}{\partial y} + \frac{\partial v}{\partial x} \end{Bmatrix} = \begin{Bmatrix} -z\,\frac{\partial \phi_x}{\partial x} \\ -z\,\frac{\partial \phi_y}{\partial y} \\ -z\left(\frac{\partial \phi_x}{\partial y} + \frac{\partial \phi_y}{\partial x}\right) \end{Bmatrix}, \tag{2}$$

$$\boldsymbol{\gamma}_\mathrm{s} = \begin{Bmatrix} \gamma_{zx} \\ \gamma_{zy} \end{Bmatrix} = \begin{Bmatrix} \frac{\partial w}{\partial x} + \frac{\partial u}{\partial z} \\ \frac{\partial w}{\partial y} + \frac{\partial v}{\partial z} \end{Bmatrix} = \begin{Bmatrix} \frac{\partial w}{\partial x} - \phi_x \\ \frac{\partial w}{\partial y} - \phi_y \end{Bmatrix}. \tag{3}$$

Table 2
Nomenclature for Section 5.

Symbol	Meaning
A_e	Area of element e
$\boldsymbol{B}_\mathrm{b}$, $\boldsymbol{B}_\mathrm{s}$	Strain–displacement matrices
$\boldsymbol{f}$	Equivalent nodal forces for the whole structure
$\boldsymbol{f}^e$	Equivalent nodal forces of element e
$\boldsymbol{K}$	Global stiffness matrix
$\boldsymbol{K}^e$, $\boldsymbol{K}^e_\mathrm{b}$, $\boldsymbol{K}^e_\mathrm{s}$	Element stiffness matrices
Λ^e	Potential energy of external loads for element e
$\boldsymbol{N}$	Shape functions in the global coordinates x, y
$\hat{\boldsymbol{N}}$	Shape functions in the parent coordinates ξ, η
$\boldsymbol{\Phi}^e$	Strain energy in element e
Π^e	Total potential energy in element e
$\tilde{\boldsymbol{u}}$	Nodal displacements and rotations of the whole structure
$\tilde{\boldsymbol{u}}^e$	Nodal displacements and rotations of element e
V_e	Volume associated to element e
w^e	Transverse displacement of element e
$\tilde{w}^e$	Transverse displacement evaluated at a node of element e
$\tilde{x}^e_i, \tilde{y}^e_i$	Global coordinates of node i of element e

The total curvature vector is defined by

$$\boldsymbol{\chi} = \begin{Bmatrix} \chi_x \\ \chi_y \\ \chi_{xy} \end{Bmatrix} = \begin{Bmatrix} \dfrac{\partial \phi_x}{\partial x} \\ \dfrac{\partial \phi_y}{\partial y} \\ \dfrac{\partial \phi_x}{\partial y} + \dfrac{\partial \phi_y}{\partial x} \end{Bmatrix}. \tag{4}$$

Next, it turns out to be useful to express the curvature $\boldsymbol{\chi}$ and the transverse shear strain $\boldsymbol{\gamma}_\mathrm{s}$ in terms of differential operators:

$$\boldsymbol{\chi} = \mathbb{B}_\mathrm{b}\boldsymbol{u}, \quad \text{where} \quad \mathbb{B}_\mathrm{b} = \begin{bmatrix} 0 & \dfrac{\partial}{\partial x} & 0 \\ 0 & 0 & \dfrac{\partial}{\partial y} \\ 0 & \dfrac{\partial}{\partial y} & \dfrac{\partial}{\partial x} \end{bmatrix}, \tag{5}$$

$$\boldsymbol{\gamma}_\mathrm{s} = \mathbb{B}_\mathrm{s}\boldsymbol{u}, \quad \text{where} \quad \mathbb{B}_\mathrm{s} = \begin{bmatrix} \dfrac{\partial}{\partial x} & -1 & 0 \\ \dfrac{\partial}{\partial y} & 0 & -1 \end{bmatrix}, \tag{6}$$

and $\boldsymbol{u}$ contains the unknown displacements of the plate problem

$$\boldsymbol{u} = \begin{Bmatrix} w \\ \phi_x \\ \phi_y \end{Bmatrix}. \tag{7}$$

Eqs. (2) and (4) involve the following relationship:

$$\boldsymbol{\epsilon}_\mathrm{b} = -z\boldsymbol{\chi}. \tag{8}$$

3.2. Equilibrium

The stress resultants are obtained by integrating the stresses over the plate thickness. Specifically, the normal bending moments M_x and M_y (for the x- and y-directions, respectively), and the twisting moment M_{xy} are defined as

$$\boldsymbol{M} = \begin{Bmatrix} M_x \\ M_y \\ M_{xy} \end{Bmatrix} = -\int_{-t/2}^{t/2} z \begin{Bmatrix} \sigma_x \\ \sigma_y \\ \tau_{xy} \end{Bmatrix} dz. \tag{9}$$

Analogously, the transverse shear forces are given by

$$\boldsymbol{Q} = \begin{Bmatrix} Q_x \\ Q_y \end{Bmatrix} = \int_{-t/2}^{t/2} \begin{Bmatrix} \tau_{zx} \\ \tau_{zy} \end{Bmatrix} dz. \tag{10}$$

In Eqs. (9) and (10), σ_x, σ_y, τ_{xy}, τ_{zx}, and τ_{zy} are components of the Cauchy stress tensor. The stress resultants satisfy the following equilibrium equations:

$$\begin{aligned}
&\frac{\partial Q_x}{\partial x} + \frac{\partial Q_y}{\partial y} + q = 0,\\
&\frac{\partial M_x}{\partial x} + \frac{\partial M_{xy}}{\partial y} + Q_x = 0,\\
&\frac{\partial M_{yx}}{\partial x} + \frac{\partial M_y}{\partial y} + Q_y = 0,
\end{aligned} \tag{11}$$

where q is the transverse distributed load oriented upward along the z-axis. Aside from q, no other external loads are considered.

3.3. Elastic constitutive laws

The constitutive equations correlate the elastic generalized strains ($\boldsymbol{\chi}^{\mathrm{el}}$ and $\boldsymbol{\gamma}_{\mathrm{s}}^{\mathrm{el}}$) with the stress resultants ($\boldsymbol{M}$ and $\boldsymbol{Q}$), both in local and nonlocal elasticity. The elastic curvature $\boldsymbol{\chi}^{\mathrm{el}}$ and the elastic shear strain $\boldsymbol{\gamma}_{\mathrm{s}}^{\mathrm{el}}$ satisfy the following relations

$$\begin{aligned}
&\boldsymbol{\chi}^{\mathrm{el}} = \boldsymbol{\chi} - \boldsymbol{\chi}^{\mathrm{in}},\\
&\boldsymbol{\gamma}_{\mathrm{s}}^{\mathrm{el}} = \boldsymbol{\gamma}_{\mathrm{s}} - \boldsymbol{\gamma}_{\mathrm{s}}^{\mathrm{in}},
\end{aligned} \tag{12}$$

where $\boldsymbol{\chi}^{\mathrm{in}}$ and $\boldsymbol{\gamma}_{\mathrm{s}}^{\mathrm{in}}$ are the inelastic curvature and the inelastic transverse shear strain, respectively. The elastic generalized strains $\boldsymbol{\chi}^{\mathrm{el}}$ and $\boldsymbol{\gamma}_{\mathrm{s}}^{\mathrm{el}}$ are denoted by $\boldsymbol{\chi}^{\mathrm{lc}}$ and $\boldsymbol{\gamma}_{\mathrm{s}}^{\mathrm{lc}}$, respectively, in the local elasticity theory outlined in Section 3.3.1. Within the elasticity theory based on the local–nonlocal mixture discussed in Section 3.3.2, the elastic generalized strains $\boldsymbol{\chi}^{\mathrm{el}}$ and $\boldsymbol{\gamma}_{\mathrm{s}}^{\mathrm{el}}$ are indicated by $\boldsymbol{\chi}^{\mathrm{mix}}$ and $\boldsymbol{\gamma}_{\mathrm{s}}^{\mathrm{mix}}$, respectively. Moreover, the strain–curvature relationship for elastic and inelastic fields is given by:

$$\boldsymbol{\varepsilon}_{\mathrm{b}}^{\mathrm{type}} = -z\,\boldsymbol{\chi}^{\mathrm{type}}, \tag{13}$$

where $\mathrm{type} = \mathrm{el}, \mathrm{in}$.

3.3.1. Local elasticity for plates

For a homogeneous isotropic linear elastic material, the pointwise constitutive law responsible for bending and twisting deformations in local analysis is

$$\boldsymbol{\sigma}_{\mathrm{b}} = \boldsymbol{C}_{\mathrm{b}}\,\boldsymbol{\varepsilon}_{\mathrm{b}}^{\mathrm{lc}}, \tag{14}$$

where

$$\boldsymbol{\sigma}_{\mathrm{b}} = \begin{Bmatrix} \sigma_x \\ \sigma_y \\ \tau_{xy} \end{Bmatrix}, \quad \boldsymbol{C}_{\mathrm{b}} = \frac{E}{1-\nu^2}\begin{bmatrix} 1 & \nu & 0 \\ \nu & 1 & 0 \\ 0 & 0 & \frac{(1-\nu)}{2} \end{bmatrix}, \quad \boldsymbol{\varepsilon}_{\mathrm{b}}^{\mathrm{lc}} = \begin{Bmatrix} \varepsilon_x^{\mathrm{lc}} \\ \varepsilon_y^{\mathrm{lc}} \\ \gamma_{xy}^{\mathrm{lc}} \end{Bmatrix}. \tag{15}$$

In Eq. (15), E and ν are the Young's modulus and the Poisson's ratio, respectively. The local elastic strain $\boldsymbol{\varepsilon}_{\mathrm{b}}^{\mathrm{lc}}$ can also be expressed in terms of the local curvature $\boldsymbol{\chi}^{\mathrm{lc}}$:

$$\boldsymbol{\varepsilon}_{\mathrm{b}}^{\mathrm{lc}} = -z\begin{Bmatrix} \chi_x^{\mathrm{lc}} \\ \chi_y^{\mathrm{lc}} \\ \chi_{xy}^{\mathrm{lc}} \end{Bmatrix} = -z\,\boldsymbol{\chi}^{\mathrm{lc}}. \tag{16}$$

The pointwise constitutive law between shear stress $\boldsymbol{\tau}_{\mathrm{s}}$ and local elastic shear strain $\boldsymbol{\gamma}_{\mathrm{s}}^{\mathrm{lc}}$ is given by

$$\boldsymbol{\tau}_{\mathrm{s}} = \boldsymbol{C}_{\mathrm{s}}\,\boldsymbol{\gamma}_{\mathrm{s}}^{\mathrm{lc}}, \tag{17}$$

where

$$\boldsymbol{\tau}_{\mathrm{s}} = \begin{Bmatrix} \tau_{zx} \\ \tau_{zy} \end{Bmatrix}, \quad \boldsymbol{C}_{\mathrm{s}} = \kappa\begin{bmatrix} G & 0 \\ 0 & G \end{bmatrix}, \quad \boldsymbol{\gamma}_{\mathrm{s}}^{\mathrm{lc}} = \begin{Bmatrix} \gamma_{zx}^{\mathrm{lc}} \\ \gamma_{zy}^{\mathrm{lc}} \end{Bmatrix}. \tag{18}$$

In Eq. (18), G is the shear modulus and κ is the shear correction factor. Taking into account Eqs. (9), (14), and (16), the sectional-level constitutive law for bending and twisting in local analysis is

$$\boldsymbol{M} = \int_{-t/2}^{t/2} z^2\,\boldsymbol{C}_{\mathrm{b}}\,\boldsymbol{\chi}^{\mathrm{lc}}\,dz = \boldsymbol{D}_{\mathrm{b}}\,\boldsymbol{\chi}^{\mathrm{lc}}, \quad \text{where} \quad \boldsymbol{D}_{\mathrm{b}} = \frac{t^3}{12}\,\boldsymbol{C}_{\mathrm{b}}. \tag{19}$$

Using Eqs. (10) and (17), the sectional-level constitutive law for shear deformations in local analysis is

$$\boldsymbol{Q} = \int_{-t/2}^{t/2} \boldsymbol{C}_{\mathrm{s}}\,\boldsymbol{\gamma}_{\mathrm{s}}^{\mathrm{lc}}\,dz = \boldsymbol{D}_{\mathrm{s}}\,\boldsymbol{\gamma}_{\mathrm{s}}^{\mathrm{lc}}, \quad \text{where} \quad \boldsymbol{D}_{\mathrm{s}} = t\,\boldsymbol{C}_{\mathrm{s}}. \tag{20}$$

By considering Eqs. (5), (6), and (12), the final sectional-level constitutive laws in local analysis are

$$\boldsymbol{M} = \boldsymbol{D}_{\mathrm{b}} \left(\mathbb{B}_{\mathrm{b}} \boldsymbol{u} - \boldsymbol{\chi}^{\mathrm{in}} \right), \tag{21}$$

$$\boldsymbol{Q} = \boldsymbol{D}_{\mathrm{s}} \left(\mathbb{B}_{\mathrm{s}} \boldsymbol{u} - \boldsymbol{\gamma}_{\mathrm{s}}^{\mathrm{in}} \right). \tag{22}$$

3.3.2. Two-phase local–nonlocal model for nanoplates

The nonlocal generalized strains $\boldsymbol{\chi}^{\mathrm{nl}}$ and $\boldsymbol{\gamma}^{\mathrm{nl}}$ at a reference point (x, y) in the nanoplate depend not only on the stress resultants $\boldsymbol{M}$ and $\boldsymbol{Q}$ at (x, y), but also on the stress resultants at all other points in the nanoplate. These nonlocal relationships are defined by the following integral convolutions:

$$\begin{aligned} \boldsymbol{\chi}^{\mathrm{nl}}(x,y) &= \begin{Bmatrix} \chi_x^{\mathrm{nl}} \\ \chi_y^{\mathrm{nl}} \\ \chi_{xy}^{\mathrm{nl}} \end{Bmatrix} = \int_A \psi \left(x - x', y - y', L_c \right) \boldsymbol{D}_{\mathrm{b}}^{-1} \boldsymbol{M} \left(x', y' \right) dx' dy' \\ &= \left(\psi * \boldsymbol{D}_{\mathrm{b}}^{-1} \boldsymbol{M} \right)(x,y) = \left(\psi * \boldsymbol{\chi}^{\mathrm{lc}} \right)(x,y), \end{aligned} \tag{23}$$

$$\begin{aligned} \boldsymbol{\gamma}_{\mathrm{s}}^{\mathrm{nl}}(x,y) &= \begin{Bmatrix} \gamma_{zx}^{\mathrm{nl}} \\ \gamma_{zy}^{\mathrm{nl}} \end{Bmatrix} = \int_A \psi \left(x - x', y - y', L_c \right) \boldsymbol{D}_{\mathrm{s}}^{-1} \boldsymbol{Q} \left(x', y' \right) dx' dy' \\ &= \left(\psi * \boldsymbol{D}_{\mathrm{s}}^{-1} \boldsymbol{Q} \right)(x,y) = \left(\psi * \boldsymbol{\gamma}_{\mathrm{s}}^{\mathrm{lc}} \right)(x,y), \end{aligned} \tag{24}$$

where A denotes the mid-plane domain (plate planform), ψ is a kernel function (Eringen, 1983), and L_c is a length-scale parameter; see Appendix A for details.

If the elastic generalized strains are defined by Eqs. (23) and (24), the resulting formulation corresponds to a purely nonlocal model. Despite their success, purely nonlocal models may exhibit excessive stiffness hardening, sensitivity to boundary conditions, and convergence difficulties, particularly in numerical implementations, as will be shown in Section 6. In recent years, local–nonlocal mixture theories have emerged as a robust, physically meaningful framework for overcoming some of the limitations of purely nonlocal models. In mixture models, the mechanical response is governed by a convex combination of local and nonlocal contributions, modulated by a weighting parameter that controls the relative influence of long-range interactions. This approach preserves the well-posedness of the governing equations while retaining the ability to model size effects, and has been successfully applied to a wide range of nanostructural problems. In this work, the elastic generalized strains are given by the following constitutive model:

$$\begin{aligned} \boldsymbol{\chi}^{\mathrm{mix}} &= \alpha \boldsymbol{\chi}^{\mathrm{lc}} + (1-\alpha) \boldsymbol{\chi}^{\mathrm{nl}}, \\ \boldsymbol{\gamma}_{\mathrm{s}}^{\mathrm{mix}} &= \alpha \boldsymbol{\gamma}_{\mathrm{s}}^{\mathrm{lc}} + (1-\alpha) \boldsymbol{\gamma}_{\mathrm{s}}^{\mathrm{nl}}, \end{aligned} \tag{25}$$

where $\alpha \in [0, 1]$. The limiting cases $\alpha = 0$ and $\alpha = 1$ correspond to the purely nonlocal and purely local models, respectively. The local–nonlocal mixture is obtained for intermediate values $0 < \alpha < 1$.

4. Iterative method for nonlocal elastostatic problems of nanoplates

The problem of nanoplates governed by the local–nonlocal constitutive laws in Eq. (25) involves integro-partial differential equations difficult to solve. Next, a solution procedure is proposed to solve nonlocal nanoplates. The proposed procedure is quite general, as it can be applied to nanoplates with arbitrary geometry and convolution kernels under various kinematic boundary and loading conditions. The procedure determines the nonlocal solution by solving a sequence of linear elastic problems, i.e., local plates. To this end, a local elastostatic operator P_{lc} is firstly defined. P_{lc} determines the displacement $\boldsymbol{u}$ of the local elastic plate (according to the Mindlin plate theory described in Sections 3.1, 3.2, and 3.3.1) subjected to the distributed transverse load q and the inelastic generalized strains $\boldsymbol{\chi}^{\mathrm{in}}$ and $\boldsymbol{\gamma}_{\mathrm{s}}^{\mathrm{in}}$:

$$\boldsymbol{u} = P_{\mathrm{lc}} \left(q, \boldsymbol{\chi}^{\mathrm{in}}, \boldsymbol{\gamma}_{\mathrm{s}}^{\mathrm{in}} \right). \tag{26}$$

Then, the operator P_{lc} is embedded within the iterative procedure described in Box I, which, upon convergence, provides the stress-driven solution for Mindlin nanoplates.

The iteration process in Box I terminates when $r^{(i)}$ becomes smaller than a given convergence tolerance $tol < 1$. Specifically,

$$r^{(i)} = \max \left(r_x^{(i)}, r_y^{(i)}, r_{xy}^{(i)}, r_{zx}^{(i)}, r_{zy}^{(i)} \right) < tol, \tag{37}$$

where

$$r_j^{(i)} = \begin{cases} \dfrac{\displaystyle\int_A \left| \left(\mathbb{B}_{\mathrm{b}} \boldsymbol{u}^{(i)} \right)_j - \left[\alpha \left(\boldsymbol{\chi}^{\mathrm{lc}\,(i)} \right)_j + (1-\alpha) \left(\psi * \boldsymbol{\chi}^{\mathrm{lc}\,(i)} \right)_j \right] \right| dA}{\displaystyle\int_A \left| \left(\mathbb{B}_{\mathrm{b}} \boldsymbol{u}^{(i)} \right)_j \right| dA} & \text{for} \quad j = x,\ y,\ xy, \\ \dfrac{\displaystyle\int_A \left| \left(\mathbb{B}_{\mathrm{s}} \boldsymbol{u}^{(i)} \right)_j - \left[\alpha \left(\boldsymbol{\gamma}_{\mathrm{s}}^{\mathrm{lc}\,(i)} \right)_j + (1-\alpha) \left(\psi * \boldsymbol{\gamma}_{\mathrm{s}}^{\mathrm{lc}\,(i)} \right)_j \right] \right| dA}{\displaystyle\int_A \left| \left(\mathbb{B}_{\mathrm{s}} \boldsymbol{u}^{(i)} \right)_j \right| dA} & \text{for} \quad j = zx,\ zy. \end{cases} \tag{38}$$

Box I. The iterative method proposed for the stress-driven integral form of nonlocal elasticity.

Iteration 0. Evaluate the initial guess:

a. Determine the local displacement solution $\Delta\boldsymbol{u}^{(0)}$ due to the external distributed transverse load q:

$$\Delta\boldsymbol{u}^{(0)} = P_{\mathrm{lc}}\left(q, \chi^{\mathrm{in}} = \boldsymbol{0}, \boldsymbol{\gamma}_{\mathrm{s}}^{\mathrm{in}} = \boldsymbol{0}\right). \tag{27}$$

b. Evaluate the local elastic generalized strains corresponding to $\Delta\boldsymbol{u}^{(0)}$:

$$\Delta\chi^{\mathrm{lc}\,(0)} = \mathbb{B}_{\mathrm{b}}\Delta\boldsymbol{u}^{(0)},\ \Delta\boldsymbol{\gamma}_{\mathrm{s}}^{\mathrm{lc}\,(0)} = \mathbb{B}_{\mathrm{s}}\Delta\boldsymbol{u}^{(0)}. \tag{28}$$

c. Initialize total displacement, local elastic generalized strains, and stress resultants:

$$\begin{aligned} &\boldsymbol{u}^{(0)} = \Delta\boldsymbol{u}^{(0)},\\ &\chi^{\mathrm{lc}\,(0)} = \Delta\chi^{\mathrm{lc}\,(0)}, \quad \boldsymbol{M}^{(0)} = \boldsymbol{D}_{\mathrm{b}}\Delta\chi^{\mathrm{lc}\,(0)},\\ &\boldsymbol{\gamma}_{\mathrm{s}}^{\mathrm{lc}\,(0)} = \Delta\boldsymbol{\gamma}_{\mathrm{s}}^{\mathrm{lc}\,(0)}, \quad \boldsymbol{Q}^{(0)} = \boldsymbol{D}_{\mathrm{s}}\Delta\boldsymbol{\gamma}_{\mathrm{s}}^{\mathrm{lc}\,(0)}. \end{aligned} \tag{29}$$

d. Set $i = 0$. Assign $r^{(0)} = 1$ and set a tolerance $tol < 1$ to enable the continuation of the iteration procedure.

Next iterations. While $r^{(i)} \geq tol$ do:

a. Increment the loop index: $i = i + 1$.

b. Evaluate the nonlocal elastic generalized strains through Eqs. (23) and (24):

$$\begin{aligned} &\Delta\chi^{\mathrm{nl}\,(i)} = \psi * \Delta\chi^{\mathrm{lc}\,(i-1)},\\ &\Delta\boldsymbol{\gamma}_{\mathrm{s}}^{\mathrm{nl}\,(i)} = \psi * \Delta\boldsymbol{\gamma}_{\mathrm{s}}^{\mathrm{lc}\,(i-1)}, \end{aligned} \tag{30}$$

and the elastic generalized strains through Eq. (25):

$$\begin{aligned} &\Delta\chi^{\mathrm{mix}\,(i)} = \alpha\,\Delta\chi^{\mathrm{lc}\,(i-1)} + (1-\alpha)\,\Delta\chi^{\mathrm{nl}\,(i)},\\ &\Delta\boldsymbol{\gamma}_{\mathrm{s}}^{\mathrm{mix}\,(i)} = \alpha\,\Delta\boldsymbol{\gamma}_{\mathrm{s}}^{\mathrm{lc}\,(i-1)} + (1-\alpha)\,\Delta\boldsymbol{\gamma}_{\mathrm{s}}^{\mathrm{nl}\,(i)}. \end{aligned} \tag{31}$$

c. Evaluate the residual generalized strains χ^{res} and $\boldsymbol{\gamma}_{\mathrm{s}}^{\mathrm{res}}$ at the ith iteration:

$$\chi^{\mathrm{res}\,(i)} = \Delta\chi^{\mathrm{mix}\,(i)} - \Delta\chi^{\mathrm{lc}\,(i-1)} = (1-\alpha)\left(\Delta\chi^{\mathrm{nl}\,(i)} - \Delta\chi^{\mathrm{lc}\,(i-1)}\right), \tag{32}$$

$$\boldsymbol{\gamma}_{\mathrm{s}}^{\mathrm{res}\,(i)} = \Delta\boldsymbol{\gamma}_{\mathrm{s}}^{\mathrm{mix}\,(i)} - \Delta\boldsymbol{\gamma}_{\mathrm{s}}^{\mathrm{lc}\,(i-1)} = (1-\alpha)\left(\Delta\boldsymbol{\gamma}_{\mathrm{s}}^{\mathrm{nl}\,(i)} - \Delta\boldsymbol{\gamma}_{\mathrm{s}}^{\mathrm{lc}\,(i-1)}\right). \tag{33}$$

d. Solve the plate subjected to inelastic generalized strains $\chi^{\mathrm{in}\,(i)}$ and $\boldsymbol{\gamma}_{\mathrm{s}}^{\mathrm{in}\,(i)}$ assumed equal to the residuals $\chi^{\mathrm{res}\,(i)}$ and $\boldsymbol{\gamma}_{\mathrm{s}}^{\mathrm{res}\,(i)}$, respectively:

$$\begin{aligned} &\chi^{\mathrm{in}\,(i)} = \chi^{\mathrm{res}\,(i)},\ \boldsymbol{\gamma}_{\mathrm{s}}^{\mathrm{in}\,(i)} = \boldsymbol{\gamma}_{\mathrm{s}}^{\mathrm{res}\,(i)},\\ &\Delta\boldsymbol{u}^{(i)} = P_{\mathrm{lc}}\left(q = 0, \chi^{\mathrm{in}\,(i)}, \boldsymbol{\gamma}_{\mathrm{s}}^{\mathrm{in}\,(i)}\right). \end{aligned} \tag{34}$$

e. Evaluate the local elastic generalized strains and stress resultants corresponding to $\Delta\boldsymbol{u}^{(i)}$ and the prescribed inelastic strains $\chi^{\mathrm{in}\,(i)}$ and $\boldsymbol{\gamma}_{\mathrm{s}}^{\mathrm{in}\,(i)}$:

$$\begin{aligned} &\Delta\chi^{\mathrm{lc}\,(i)} = \mathbb{B}_{\mathrm{b}}\Delta\boldsymbol{u}^{(i)} - \chi^{\mathrm{in}\,(i)}, \quad \Delta\boldsymbol{M}^{(i)} = \boldsymbol{D}_{\mathrm{b}}\Delta\chi^{\mathrm{lc}\,(i)},\\ &\Delta\boldsymbol{\gamma}_{\mathrm{s}}^{\mathrm{lc}\,(i)} = \mathbb{B}_{\mathrm{s}}\Delta\boldsymbol{u}^{(i)} - \boldsymbol{\gamma}_{\mathrm{s}}^{\mathrm{in}\,(i)}, \quad \Delta\boldsymbol{Q}^{(i)} = \boldsymbol{D}_{\mathrm{s}}\Delta\boldsymbol{\gamma}_{\mathrm{s}}^{\mathrm{lc}\,(i)}. \end{aligned} \tag{35}$$

f. Update total displacement, local elastic generalized strains, and stress resultants:

$$\begin{aligned} &\boldsymbol{u}^{(i)} = \boldsymbol{u}^{(i-1)} + \Delta\boldsymbol{u}^{(i)},\\ &\chi^{\mathrm{lc}\,(i)} = \chi^{\mathrm{lc}\,(i-1)} + \Delta\chi^{\mathrm{lc}\,(i)}, \quad \boldsymbol{M}^{(i)} = \boldsymbol{M}^{(i-1)} + \Delta\boldsymbol{M}^{(i)},\\ &\boldsymbol{\gamma}_{\mathrm{s}}^{\mathrm{lc}\,(i)} = \boldsymbol{\gamma}_{\mathrm{s}}^{\mathrm{lc}\,(i-1)} + \Delta\boldsymbol{\gamma}_{\mathrm{s}}^{\mathrm{lc}\,(i)}, \quad \boldsymbol{Q}^{(i)} = \boldsymbol{Q}^{(i-1)} + \Delta\boldsymbol{Q}^{(i)}. \end{aligned} \tag{36}$$

g. Calculate the residual $r^{(i)}$ accordingly to Eq. (37).

The components appearing in the integrals of Eq. (38) belong to the following vectors:

$$\begin{aligned}
&\mathbb{B}_{\mathrm{b}}\boldsymbol{u}^{(i)} = \left[\left(\mathbb{B}_{\mathrm{b}}\boldsymbol{u}^{(i)}\right)_x,\ \left(\mathbb{B}_{\mathrm{b}}\boldsymbol{u}^{(i)}\right)_y,\ \left(\mathbb{B}_{\mathrm{b}}\boldsymbol{u}^{(i)}\right)_{xy}\right]^{\mathrm{T}},\\
&\mathbb{B}_{\mathrm{s}}\boldsymbol{u}^{(i)} = \left[\left(\mathbb{B}_{\mathrm{s}}\boldsymbol{u}^{(i)}\right)_{zx},\ \left(\mathbb{B}_{\mathrm{s}}\boldsymbol{u}^{(i)}\right)_{zy}\right]^{\mathrm{T}},\\
&\psi * \boldsymbol{\chi}^{\mathrm{lc}\,(i)} = \left[\left(\psi * \boldsymbol{\chi}^{\mathrm{lc}\,(i)}\right)_x,\ \left(\psi * \boldsymbol{\chi}^{\mathrm{lc}\,(i)}\right)_y,\ \left(\psi * \boldsymbol{\chi}^{\mathrm{lc}\,(i)}\right)_{xy}\right]^{\mathrm{T}},\\
&\psi * \boldsymbol{\gamma}_{\mathrm{s}}^{\mathrm{lc}\,(i)} = \left[\left(\psi * \boldsymbol{\gamma}_{\mathrm{s}}^{\mathrm{lc}\,(i)}\right)_{zx},\ \left(\psi * \boldsymbol{\gamma}_{\mathrm{s}}^{\mathrm{lc}\,(i)}\right)_{zy}\right]^{\mathrm{T}}.
\end{aligned} \tag{39}$$

In Eqs. (30) and (39), the dependence on (x, y) of the convolution is omitted for brevity. In Eq. (39), $\mathbb{B}_{\mathrm{b}}\boldsymbol{u}^{(i)}$ and $\mathbb{B}_{\mathrm{s}}\boldsymbol{u}^{(i)}$ represent the total curvature and shear strain, respectively, of the deformed nanoplate at the end of the current iteration i. The generalized strains $\mathbb{B}_{\mathrm{b}}\boldsymbol{u}^{(i)}$ and $\mathbb{B}_{\mathrm{s}}\boldsymbol{u}^{(i)}$ have to be very close to the local–nonlocal mixtures of the curvature and the shear strain, respectively, after reaching convergence. Indeed, in the proposed method, the local–nonlocal constitutive laws in Eq. (25) are not satisfied but only approximated with a prescribed level of precision, after a certain number of iterations, as controlled by the convergence criterion in Eq. (37). The fulfillment of the kinematic and equilibrium equations of the problem is guaranteed at each iteration of the procedure.

5. Finite element solution

The finite element method (FEM) provides a flexible and powerful framework for the analysis of shear-deformable nanoplates. However, the direct implementation of nonlocal operators within FEM formulations often increases computational cost and complexity. An effective alternative is FEM-based iterative strategies, which reformulate the nonlocal problem as a sequence of local-like problems, enabling the use of standard finite element technology while ensuring numerical stability and convergence.

FEM is used in Section 5.1 to obtain the local elastostatic operator P_{lc} defined in Eq. (26) and employed in Box I. The nonlocal generalized strains in Eqs. (23) and (24) are also evaluated within the FEM-based procedure described in Section 5.2.

5.1. The local elastostatic operator

In the FEM framework, the geometric domain of the plate mid-plane is partitioned into a finite set of non-overlapping subdomains, termed finite elements. The generic element of this partition (mesh) is a quadrilateral with n nodes. The finite element approximation of the displacement $\boldsymbol{u}$ of the generic element e is

$$\boldsymbol{u}^e(x,y) = \begin{Bmatrix} w^e(x,y) \\ \phi_x^e(x,y) \\ \phi_y^e(x,y) \end{Bmatrix} = \sum_{a=1}^{n} N_a(x,y)\,\tilde{\boldsymbol{u}}_a^e = \boldsymbol{N}(x,y)\,\tilde{\boldsymbol{u}}^e, \tag{40}$$

where

$$\boldsymbol{N}(x,y) = \left[\boldsymbol{N}_1(x,y), \boldsymbol{N}_2(x,y), \dots, \boldsymbol{N}_n(x,y)\right], \quad \tilde{\boldsymbol{u}}^e = \left[\left(\tilde{\boldsymbol{u}}_1^e\right)^{\mathrm{T}}, \left(\tilde{\boldsymbol{u}}_2^e\right)^{\mathrm{T}}, \dots, \left(\tilde{\boldsymbol{u}}_n^e\right)^{\mathrm{T}}\right]^{\mathrm{T}} \tag{41}$$

and

$$\boldsymbol{N}_a(x,y) = \begin{bmatrix} N_a(x,y) & 0 & 0 \\ 0 & N_a(x,y) & 0 \\ 0 & 0 & N_a(x,y) \end{bmatrix}, \quad \tilde{\boldsymbol{u}}_a^e = \left[(\tilde{w}^e)_a, \left(\tilde{\phi}_x^e\right)_a, \left(\tilde{\phi}_y^e\right)_a\right]^{\mathrm{T}}. \tag{42}$$

In Eq. (40), w^e, ϕ_x^e, and ϕ_y^e correspond to the displacements w, ϕ_x, and ϕ_y appearing in (7), $\tilde{\boldsymbol{u}}_a^e$ is the displacement vector at node a of element e, and N_a is the shape function associated to node a. The vector $\tilde{\boldsymbol{u}}_a^e$ contains the nodal parameters of displacement and rotation: $(\tilde{w}^e)_a$, $\left(\tilde{\phi}_x^e\right)_a$, and $\left(\tilde{\phi}_y^e\right)_a$ are, respectively, the transverse displacement w, the rotation ϕ_x around the y-axis, and the rotation ϕ_y around the x-axis evaluated at node a in finite element e. The unknowns of the problem are the nodal displacements grouped in the vector $\tilde{\boldsymbol{u}}^e$. The shape functions N_a also depend on the element e, but the superscript e on the symbol N_a and on other objects referring to the element e is omitted. Next, the dependence on (x, y) is also omitted for the sake of brevity. See Appendix B for the adopted finite elements and shape functions.

The strain vectors are

$$\begin{aligned}
&\boldsymbol{\epsilon}_{\mathrm{b}} = -z\,\mathbb{B}_{\mathrm{b}}\boldsymbol{u}^e = -z\,\boldsymbol{B}_{\mathrm{b}}\tilde{\boldsymbol{u}}^e,\\
&\boldsymbol{\gamma}_{\mathrm{s}} = \mathbb{B}_{\mathrm{s}}\boldsymbol{u}^e = \boldsymbol{B}_{\mathrm{s}}\tilde{\boldsymbol{u}}^e,
\end{aligned} \tag{43}$$

where

$$\begin{aligned}
&\boldsymbol{B}_{\mathrm{b}} = \left[\mathbb{B}_{\mathrm{b}}\boldsymbol{N}_1, \mathbb{B}_{\mathrm{b}}\boldsymbol{N}_2, \dots, \mathbb{B}_{\mathrm{b}}\boldsymbol{N}_n\right], \quad \mathbb{B}_{\mathrm{b}}\boldsymbol{N}_a = \begin{bmatrix} 0 & \frac{\partial N_a}{\partial x} & 0 \\ 0 & 0 & \frac{\partial N_a}{\partial y} \\ 0 & \frac{\partial N_a}{\partial y} & \frac{\partial N_a}{\partial x} \end{bmatrix},\\
&\boldsymbol{B}_{\mathrm{s}} = \left[\mathbb{B}_{\mathrm{s}}\boldsymbol{N}_1, \mathbb{B}_{\mathrm{s}}\boldsymbol{N}_2, \dots, \mathbb{B}_{\mathrm{s}}\boldsymbol{N}_n\right], \quad \mathbb{B}_{\mathrm{s}}\boldsymbol{N}_a = \begin{bmatrix} \frac{\partial N_a}{\partial x} & -N_a & 0 \\ \frac{\partial N_a}{\partial y} & 0 & -N_a \end{bmatrix}.
\end{aligned} \tag{44}$$

The total potential energy (TPE) of the element e is given by

$$\Pi^e = \Phi^e + \Lambda^e, \tag{45}$$

where Φ^e is the strain energy associated with bending, twisting, and shear deformations

$$\begin{aligned}\Phi^e &= \frac{1}{2}\int_{V_e} \left(\boldsymbol{\varepsilon}_{\mathrm{b}}^{\mathrm{lc}}\right)^{\mathrm{T}} \boldsymbol{C}_{\mathrm{b}} \boldsymbol{\varepsilon}_{\mathrm{b}}^{\mathrm{lc}}\, dV + \frac{1}{2}\int_{V_e} \left(\boldsymbol{\gamma}_{\mathrm{s}}^{\mathrm{lc}}\right)^{\mathrm{T}} \boldsymbol{C}_{\mathrm{s}} \boldsymbol{\gamma}_{\mathrm{s}}^{\mathrm{lc}} dV \\ &= \frac{1}{2}\int_{V_e} \left(\boldsymbol{\varepsilon}_{\mathrm{b}} - \boldsymbol{\varepsilon}_{\mathrm{b}}^{\mathrm{in}}\right)^{\mathrm{T}} \boldsymbol{C}_{\mathrm{b}} \left(\boldsymbol{\varepsilon}_{\mathrm{b}} - \boldsymbol{\varepsilon}_{\mathrm{b}}^{\mathrm{in}}\right) dV + \frac{1}{2}\int_{V_e} \left(\boldsymbol{\gamma}_{\mathrm{s}} - \boldsymbol{\gamma}_{\mathrm{s}}^{\mathrm{in}}\right)^{\mathrm{T}} \boldsymbol{C}_{\mathrm{s}} \left(\boldsymbol{\gamma}_{\mathrm{s}} - \boldsymbol{\gamma}_{\mathrm{s}}^{\mathrm{in}}\right) dV,\end{aligned} \tag{46}$$

and Λ^e is the opposite of the external work:

$$\Lambda^e = -\int_{A_e} w^e\, q\, dA = -\int_{A_e} (\tilde{\boldsymbol{u}}^e)^{\mathrm{T}} \boldsymbol{N}_{\mathrm{w}}^{\mathrm{T}}\, q\, dA, \tag{47}$$

where

$$\boldsymbol{N}_{\mathrm{w}} = \left[N_1, 0, 0, N_2, 0, 0, \ldots, N_n, 0, 0\right]. \tag{48}$$

In Eqs. (46) and (47), V_e is the volume corresponding to element e and A_e denotes the area of the plate mid-surface belonging to element e. Taking into account Eqs. (13), the strain energy is

$$\begin{aligned}\Phi^e = &\frac{1}{2}\int_{A_e} \left[(\tilde{\boldsymbol{u}}^e)^{\mathrm{T}} \boldsymbol{B}_{\mathrm{b}}^{\mathrm{T}} \left(\boldsymbol{D}_{\mathrm{b}} \boldsymbol{B}_{\mathrm{b}} \tilde{\boldsymbol{u}}^e - 2\boldsymbol{D}_{\mathrm{b}} \boldsymbol{\chi}^{\mathrm{in}}\right) + \left(\boldsymbol{\chi}^{\mathrm{in}}\right)^{\mathrm{T}} \boldsymbol{D}_{\mathrm{b}} \boldsymbol{\chi}^{\mathrm{in}}\right] dA \\ &+ \frac{1}{2}\int_{A_e} \left[(\tilde{\boldsymbol{u}}^e)^{\mathrm{T}} \boldsymbol{B}_{\mathrm{s}}^{\mathrm{T}} \left(\boldsymbol{D}_{\mathrm{s}} \boldsymbol{B}_{\mathrm{s}} \tilde{\boldsymbol{u}}^e - 2\boldsymbol{D}_{\mathrm{s}} \boldsymbol{\gamma}_{\mathrm{s}}^{\mathrm{in}}\right) + \left(\boldsymbol{\gamma}_{\mathrm{s}}^{\mathrm{in}}\right)^{\mathrm{T}} \boldsymbol{D}_{\mathrm{s}} \boldsymbol{\gamma}_{\mathrm{s}}^{\mathrm{in}}\right] dA.\end{aligned} \tag{49}$$

The principle of minimum total potential energy provides the following equilibrium equation of the element e:

$$\boldsymbol{K}^e \tilde{\boldsymbol{u}}^e = \boldsymbol{f}^e, \tag{50}$$

where the element stiffness matrix $\boldsymbol{K}^e$ and the equivalent nodal forces $\boldsymbol{f}^e$ for the generic element e are given by

$$\begin{aligned}&\boldsymbol{K}^e = \boldsymbol{K}_{\mathrm{b}}^e + \boldsymbol{K}_{\mathrm{s}}^e, \quad \text{with} \begin{cases} \boldsymbol{K}_{\mathrm{b}}^e = \displaystyle\int_{A_e} \boldsymbol{B}_{\mathrm{b}}^{\mathrm{T}} \boldsymbol{D}_{\mathrm{b}} \boldsymbol{B}_{\mathrm{b}}\, dA, \\ \boldsymbol{K}_{\mathrm{s}}^e = \displaystyle\int_{A_e} \boldsymbol{B}_{\mathrm{s}}^{\mathrm{T}} \boldsymbol{D}_{\mathrm{s}} \boldsymbol{B}_{\mathrm{s}}\, dA, \end{cases} \\ &\boldsymbol{f}^e = \int_{A_e} \left(\boldsymbol{B}_{\mathrm{b}}^{\mathrm{T}} \boldsymbol{D}_{\mathrm{b}} \boldsymbol{\chi}^{\mathrm{in}} + \boldsymbol{B}_{\mathrm{s}}^{\mathrm{T}} \boldsymbol{D}_{\mathrm{s}} \boldsymbol{\gamma}_{\mathrm{s}}^{\mathrm{in}}\right)\, dA + \int_{A_e} \boldsymbol{N}_{\mathrm{w}}^{\mathrm{T}}\, q\, dA.\end{aligned} \tag{51}$$

Assembling the element stiffness matrices and equivalent nodal forces provides the following global system of equations

$$\boldsymbol{K}\tilde{\boldsymbol{u}} = \boldsymbol{f}. \tag{52}$$

The solution $\tilde{\boldsymbol{u}}$ of Eq. (52) provides the unknown displacement $\boldsymbol{u}$ due to:

- the transverse load q,
- the inelastic curvature $\boldsymbol{\chi}^{\mathrm{in}}$,
- the inelastic shear strain $\boldsymbol{\gamma}_{\mathrm{s}}^{\mathrm{in}}$.

The operator P_{lc} in Eq. (26) is represented by the above-mentioned finite element procedure providing the solution $\tilde{\boldsymbol{u}}$ of Eq. (52).

The integrals in Eqs. (23), (24), and (51) are evaluated with Gaussian quadrature. Specifically, the integral over A_e is converted to an integral over the parent domain defined by $-1 \leqslant \xi, \eta \leqslant 1$. To this end, the square element defined in the parent coordinates ξ, η is transformed into the element e defined in the global coordinates x, y via the following parametric geometric mapping

$$\begin{cases} x(\xi,\eta) = \displaystyle\sum_{i=1}^{4} \hat{N}_i(\xi,\eta)\, \tilde{x}_i^e, \\ y(\xi,\eta) = \displaystyle\sum_{i=1}^{4} \hat{N}_i(\xi,\eta)\, \tilde{y}_i^e, \end{cases} \tag{53}$$

where $\hat{N}_1, \ldots, \hat{N}_4$ are the bilinear shape functions reported in Appendix B and $\left(\tilde{x}_i^e, \tilde{y}_i^e\right)$ are the (x, y) coordinates of the vertex node i, of element e, corresponding to the shape function $\hat{N}_i$. The bilinear vertex-based mapping in Eq. (53) defines an iso-parametric interpolation for the finite element Q4 and sub-parametric interpolations for the higher-order elements QL9, QL16, and QGLL16, see Appendix B.

The integral of a generic function $g = g(x, y)$ over A_e is evaluated as

$$\begin{aligned}\int_{A_e} g(x,y)\,dx\,dy &= \int_{-1}^{1}\int_{-1}^{1} \hat{g}(\xi,\eta)\,J(\xi,\eta)\,d\xi\,d\eta \\ &= \sum_{i=1}^{n_1}\sum_{j=1}^{n_2} \hat{g}\left(\xi_i,\eta_j\right) J\left(\xi_i,\eta_j\right) W_{ij},\end{aligned} \tag{54}$$

where

$$\hat{g}(\xi,\eta) = g\left(x(\xi,\eta), y(\xi,\eta)\right), \tag{55}$$

$J(\xi,\eta)$ is the Jacobian of the transformation in Eq. (53), n_1 and n_2 are the number of Gauss points along the ξ- and η-axes, respectively, $\left(\xi_i,\eta_j\right)$ is a Gauss point, and W_{ij} is the weight associated with the Gauss point $\left(\xi_i,\eta_j\right)$. Given a function $g = g(x, y)$, the symbol $\hat{g}$ will denote the composition of functions represented in Eq. (55).

5.2. FEM integral convolutions for the evaluation of the nonlocal strains

The local generalized strains $\left(\hat{\boldsymbol{\chi}}^{\mathrm{lc}}\right)^k$ and $\left(\hat{\boldsymbol{\gamma}}_{\mathrm{s}}^{\mathrm{lc}}\right)^k$ at the Gauss point $\left(\xi_l,\eta_m\right)$ of the element k are

$$\begin{aligned}\left(\hat{\boldsymbol{\chi}}^{\mathrm{lc}}\right)^k\left(\xi_l,\eta_m\right) &= \hat{\boldsymbol{B}}_{\mathrm{b}}\left(\xi_l,\eta_m\right)\tilde{\boldsymbol{u}}^k - \left(\hat{\boldsymbol{\chi}}^{\mathrm{in}}\right)^k\left(\xi_l,\eta_m\right), \\ \left(\hat{\boldsymbol{\gamma}}_{\mathrm{s}}^{\mathrm{lc}}\right)^k\left(\xi_l,\eta_m\right) &= \hat{\boldsymbol{B}}_{\mathrm{s}}\left(\xi_l,\eta_m\right)\tilde{\boldsymbol{u}}^k - \left(\hat{\boldsymbol{\gamma}}_{\mathrm{s}}^{\mathrm{in}}\right)^k\left(\xi_l,\eta_m\right).\end{aligned} \tag{56}$$

Then, the convolutions in Eqs. (23) and (24) are numerically evaluated using the Gauss quadrature, integrating over the total number n_{e} of the elements of the mesh. In particular, the nonlocal generalized strains $\left(\hat{\boldsymbol{\chi}}^{\mathrm{nl}}\right)^e$ and $\left(\hat{\boldsymbol{\gamma}}_{\mathrm{s}}^{\mathrm{nl}}\right)^e$ at the Gauss point $\left(\xi_i,\eta_j\right)$ of element e are given by

$$\begin{aligned}\left(\hat{\boldsymbol{\chi}}^{\mathrm{nl}}\right)^e\left(\xi_i,\eta_j\right) &= \sum_{k=1}^{n_{\mathrm{e}}}\sum_{l=1}^{n_1}\sum_{m=1}^{n_2} \psi\left(\Delta x_{e',k'},\Delta y_{e',k'},L_c\right)\left(\hat{\boldsymbol{\chi}}^{\mathrm{lc}}\right)^k\left(\xi_l,\eta_m\right) J^k\left(\xi_l,\eta_m\right) W_{lm}, \\ \left(\hat{\boldsymbol{\gamma}}_{\mathrm{s}}^{\mathrm{nl}}\right)^e\left(\xi_i,\eta_j\right) &= \sum_{k=1}^{n_{\mathrm{e}}}\sum_{l=1}^{n_1}\sum_{m=1}^{n_2} \psi\left(\Delta x_{e',k'},\Delta y_{e',k'},L_c\right)\left(\hat{\boldsymbol{\gamma}}_{\mathrm{s}}^{\mathrm{lc}}\right)^k\left(\xi_l,\eta_m\right) J^k\left(\xi_l,\eta_m\right) W_{lm},\end{aligned} \tag{57}$$

where

$$\begin{aligned}&\Delta x_{e',k'} = x^e\left(\xi_i,\eta_j\right) - x^k\left(\xi_l,\eta_m\right), \\ &\Delta y_{e',k'} = y^e\left(\xi_i,\eta_j\right) - y^k\left(\xi_l,\eta_m\right), \\ &e' = (e,i,j), \quad k' = (k,l,m),\end{aligned} \tag{58}$$

and $\left(x^e\left(\xi_i,\eta_j\right), y^e\left(\xi_i,\eta_j\right)\right)$ are the global coordinates in element e corresponding to the Gauss point $\left(\xi_i,\eta_j\right)$ through the transformation in Eq. (53). The same holds for the coordinates $\left(x^k\left(\xi_l,\eta_m\right),\ y^k\left(\xi_l,\eta_m\right)\right)$.

The most CPU time-consuming operation in the algorithm reported in Box I is the evaluation of the nonlocal generalized strains $\hat{\boldsymbol{\chi}}^{\mathrm{nl}}$ and $\hat{\boldsymbol{\gamma}}_{\mathrm{s}}^{\mathrm{nl}}$ through Eq. (57).

6. Case studies

The method presented in the previous sections allows analysis of nanoplates with arbitrary geometries. For simplicity, the results presented in Section 6 refer to the rectangular nanoplate shown in Fig. 2, with length, width, and thickness denoted by L_x, L_y, and t, respectively. The plate mid-plane is colored gray in Fig. 2. The Cartesian coordinate system has its origin at a vertex of the mid-plane, and the z-axis is oriented upward. The mid-plane of the nanoplates under consideration is discretized using rectangular Lagrangian finite elements; see Appendix B for a brief description of the finite elements adopted in this work. Each element of the mesh has sides with lengths $a_x = L_x/n_x$ and $a_y = L_y/n_y$ along the x- and y-axes, respectively; n_x and n_y denote the number of finite elements along the x- and y-axes, respectively, see, e.g., Fig. 3. The selective quadrature listed in Table 15 is used to avoid shear locking.

Next, the proposed iterative method is applied to determine the static state of nonlocal nanoplates with different types of kinematic boundary conditions. Specifically, the following types of nanoplates are considered:

- Clamped nanoplates (CCCC), characterized by the following boundary conditions (BCs):

$$w = \phi_x = \phi_y = 0 \quad \text{on all boundaries.} \tag{59}$$

- Simply supported nanoplates (SSSS), with the following BCs:

$$\begin{cases} w = \phi_x = 0 & \text{for } y = 0, L_y, \\ w = \phi_y = 0 & \text{for } x = 0, L_x. \end{cases} \tag{60}$$

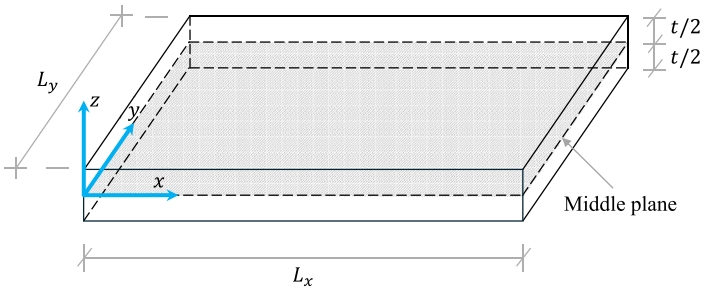

Fig. 2. Geometry of the nanoplates adopted in Section 6.

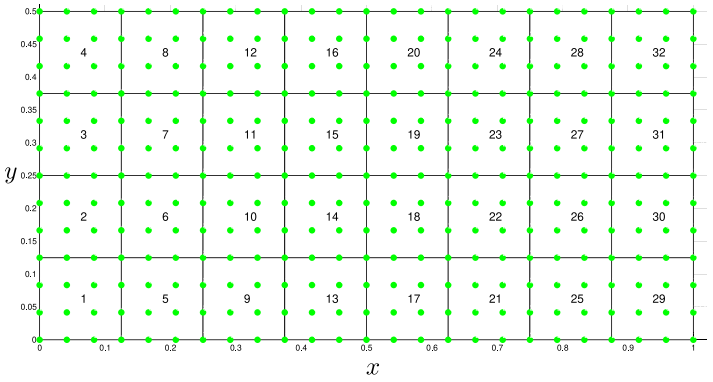

Fig. 3. A mesh composed of bi-cubic QL16 finite elements with $n_x = 8$ and $n_y = 4$.

- Nanoplates clamped along the edges parallel to the y-axis and free along the other edges; denoted by the acronym FCFC, this type of nanoplate is characterized by the following BCs:

$$w = \phi_x = \phi_y = 0 \quad \text{for } x = 0, L_x. \tag{61}$$

- Nanoplates simply supported along the edges parallel to the y-axis and free along the other edges; this type of nanoplate, denoted by the acronym FSFS, is characterized by the following BCs:

$$w = \phi_y = 0 \quad \text{for } x = 0, L_x. \tag{62}$$

In this section, the results are presented in nondimensional form. Accordingly, the dimensionless parameters defining the nonlocal plate model are introduced as

$$\lambda = \frac{L_y}{L_x},\ \lambda_c = \frac{L_c}{L_x},\ \beta^{-1} = \frac{\kappa G t L^2}{D},\ \bar{q} = \frac{qL^3}{D}, \tag{63}$$

where

$$L = L_x \geq L_y,\ D = \frac{Et^3}{12(1-\nu^2)}. \tag{64}$$

The independent dimensionless parameters defining the model are λ, λ_c, ν, α, β^{-1}, and $\bar{q}$. Moreover, it is assumed that $G = E/(2+2\nu)$ and $\kappa = 5/6$, which leads to

$$\beta^{-1} = 5\,(1-\nu)\left(\frac{L}{t}\right)^2. \tag{65}$$

For a fixed Poisson's ratio ν, the parameter β^{-1} is uniquely determined by the slenderness ratio L/t; accordingly, L/t is used in place of β^{-1} as an independent parameter. The following dimensionless variables are introduced for the presentation of the results:

$$\bar{x} = \frac{x}{L_x},\ \bar{y} = \frac{y}{L_y},\ \bar{w} = \frac{w}{L}. \tag{66}$$

It should be noted that the nondimensionalization in Eqs. (63)–(66) is limited to the presentation of the results. For convenience, some governing equations or intermediate expressions may still be reported in dimensional form.

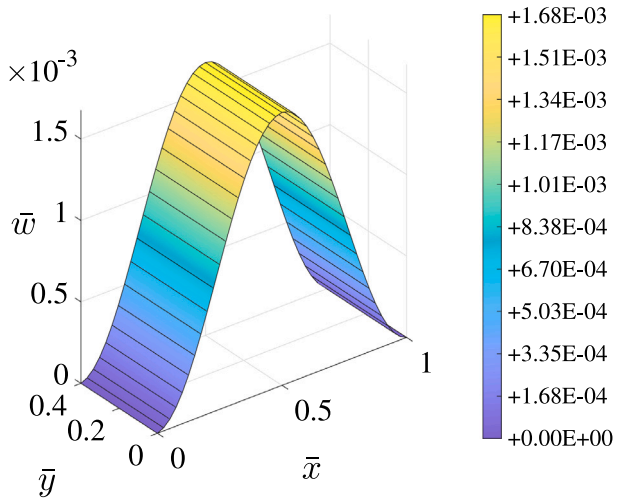

Fig. 4. Deformed configuration (dimensionless transverse displacement $\bar{w}$) for the FCFC nanoplate in cylindrical bending and characterized by $\lambda_c = 0.1$, $\alpha = 0$, $L/t = 10$, and $\bar{q} = 1$. The nanoplate is meshed with QL16 elements, $n_e = n_x = 40$, iteration $i = 5$.

6.1. Cylindrical bending of nanoplates for comparison purposes

A first validation of the proposed iterative method is performed by assuming that the nanoplate is under cylindrical bending, so that it behaves like a stress-driven nonlocal nanobeam, for which exact closed-form solutions are available for comparison. In cylindrical bending, the variables of the problem do not depend on y: the only non-zero components of $\boldsymbol{\chi}$, $\boldsymbol{\gamma}_s$, $\boldsymbol{M}$, and $\boldsymbol{Q}$ are, respectively, χ_x, γ_{zx}, M_x, and Q_x. To this end, it is assumed $\nu = 0$, and the following integral convolutions for the nonlocal generalized strains:

$$\begin{cases} \chi_x^{\mathrm{nl}}(x) = \dfrac{1}{2L_c L_y} \displaystyle\int_A \exp\left(-\frac{|x-x'|}{L_c}\right) \chi_x^{\mathrm{lc}}(x')\, dx'dy', \\ \gamma_{zx}^{\mathrm{nl}}(x) = \dfrac{1}{2L_c L_y} \displaystyle\int_A \exp\left(-\frac{|x-x'|}{L_c}\right) \gamma_{zx}^{\mathrm{lc}}(x')\, dx'dy'. \end{cases} \tag{67}$$

The nonlocal strains in Eq. (67) could also be evaluated with one-dimensional integrals. However, two-dimensional integrals are preferred in Eq. (67), also to validate the two-dimensional Gauss quadrature schemes, which will be intensively used in Section 6.2. Indeed, the ratio $1/L_y$ in Eq. (67) serves to make the two-dimensional integrals consistent with the one-dimensional convolutions involved in nonlocal beam theory (Barretta, Caporale et al., 2019). Next, FCFC and FSFS nanoplates are considered, ensuring that the boundary conditions preserve the cylindrical bending. The meshes used in this Section 6.1 have only one finite element along the y-direction, namely $n_y = 1$. A deformed configuration of the mesh of an FCFC nanoplate in cylindrical bending is shown in Fig. 4.

In Fig. 5, the dimensionless transverse displacement $\bar{w}^{(i)} = w^{(i)}/L$, with $i = 0, 1, 2$, is plotted against $\bar{x}$ for the FCFC nanoplate characterized by $\lambda_c = 0.1$, $\alpha = 0$, $\beta^{-1} = 500$ (that is $L/t = 10$), and $\bar{q} = 1$. Within the adopted iterative method, $w^{(i)}$ is the first component of the displacement vector $\boldsymbol{u}^{(i)}$ appearing in Box I. Hence, the variable $w^{(i)}/L$ denotes the dimensionless transverse displacement at iteration i. The mesh is discretized with rectangular QL16 elements; the number of finite elements along the x-axis is $n_x = 12$, which is also the total number n_e of elements of the mesh. The variable $\bar{w}^{(i)}$ is expected to tend to the exact dimensionless displacement $\bar{w}^{\mathrm{exact}}$ as i tends to ∞. Considering the analogy between the cylindrical bending of nanoplates and the one-dimensional bending of nanobeams, $\bar{w}^{\mathrm{exact}}$ is the solution of the following system of differential equations, in the unknowns $\bar{w} = \bar{w}(\bar{x})$ and $\phi_x = \phi_x(\bar{x})$, which govern the problem of two-phase local–nonlocal stress-driven Timoshenko nanobeams (Barretta, Caporale et al., 2019):

$$\begin{cases} \dfrac{d^5\phi_x}{d\bar{x}^5} - \dfrac{1}{\lambda_c^2}\dfrac{d^3\phi_x}{d\bar{x}^3} = \alpha\dfrac{d^2\bar{q}}{d\bar{x}^2} - \dfrac{\bar{q}}{\lambda_c^2}, \\ \dfrac{d^2\gamma_{zx}}{d\bar{x}^2} - \dfrac{1}{\lambda_c^2}\gamma_{zx} = -\beta\left(\alpha\dfrac{d^3\bar{M}_x}{d\bar{x}^3} - \dfrac{1}{\lambda_c^2}\dfrac{d\bar{M}_x}{d\bar{x}}\right), \end{cases} \tag{68}$$

where $\gamma_{zx} = d\bar{w}/d\bar{x} - \phi_x$ and

$$\bar{M}_x = -\lambda_c^2\left(\frac{d^3\phi_x}{d\bar{x}^3} - \frac{1}{\lambda_c^2}\frac{d\phi_x}{d\bar{x}} - \alpha\bar{q}\right). \tag{69}$$

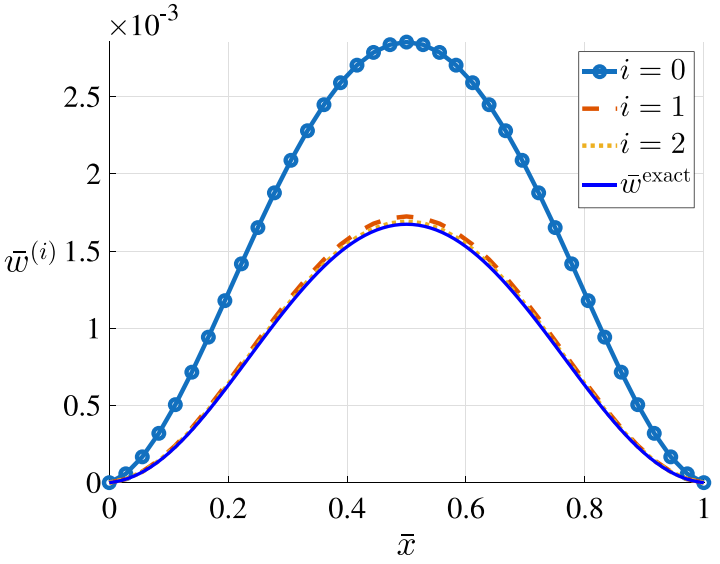

Fig. 5. Dimensionless transverse displacement $\bar{w}^{(i)}$, with $i = 0, 1, 2$, plotted against $\bar{x}$ for the FCFC nanoplate in cylindrical bending and characterized by $\lambda_c = 0.1$, $\alpha = 0$, $\beta^{-1} = 500$ (that is $L/t = 10$), $\bar{q} = 1$, and QL16 elements with $n_x = 12$.

The system in Eq. (68) needs to be accompanied by the following constitutive boundary conditions

$$\begin{cases} \left.\dfrac{d^2\phi_x}{d\bar{x}^2}\right|_{\bar{x}=0} - \dfrac{1}{\lambda_c}\left.\dfrac{d\phi_x}{d\bar{x}}\right|_{\bar{x}=0} = \alpha \left.\dfrac{d\bar{M}_x}{d\bar{x}}\right|_{\bar{x}=0} - \dfrac{\alpha}{\lambda_c}\left.\bar{M}_x\right|_{\bar{x}=0}, \\ \left.\dfrac{d^2\phi_x}{d\bar{x}^2}\right|_{\bar{x}=1} + \dfrac{1}{\lambda_c}\left.\dfrac{d\phi_x}{d\bar{x}}\right|_{\bar{x}=1} = \alpha \left.\dfrac{d\bar{M}_x}{d\bar{x}}\right|_{\bar{x}=1} + \dfrac{\alpha}{\lambda_c}\left.\bar{M}_x\right|_{\bar{x}=1}, \\ \left.\dfrac{d\gamma_{zx}}{d\bar{x}}\right|_{\bar{x}=0} - \dfrac{1}{\lambda_c}\left.\gamma_{zx}\right|_{\bar{x}=0} = -\alpha\beta \left.\dfrac{d^2\bar{M}_x}{d\bar{x}^2}\right|_{\bar{x}=0} + \dfrac{\alpha\beta}{\lambda_c}\left.\dfrac{d\bar{M}_x}{d\bar{x}}\right|_{\bar{x}=0}, \\ \left.\dfrac{d\gamma_{zx}}{d\bar{x}}\right|_{\bar{x}=1} + \dfrac{1}{\lambda_c}\left.\gamma_{zx}\right|_{\bar{x}=1} = -\alpha\beta \left.\dfrac{d^2\bar{M}_x}{d\bar{x}^2}\right|_{\bar{x}=1} - \dfrac{\alpha\beta}{\lambda_c}\left.\dfrac{d\bar{M}_x}{d\bar{x}}\right|_{\bar{x}=1}, \end{cases} \tag{70}$$

as well as the standard boundary conditions.

The approximate numerical solution $\bar{w}^{(i)}$ achieves near-perfect agreement with the exact solution $\bar{w}^{\text{exact}}$ from the very first iterations, e.g., $i = 2$.

In the adopted FEM-based iterative procedure, element-level integrations with selective quadrature are performed not only to calculate the element stiffness matrices but also to evaluate the nonlocal generalized strains and the nodal forces equivalent to the inelastic strains (see Appendix B). Thus, it is interesting to compare the results obtained by adopting different types of finite elements. In the considered nanoplates under cylindrical bending, the maximum dimensionless displacement at iteration i is given by $\bar{w}^{(i)}_{\max} = \bar{w}^{(i)}(0.5, \bar{y})$, i.e. $\bar{w}^{(i)}$ evaluated at abscissa $\bar{x} = 0.5$. Table 3 reports the maximum dimensionless displacement $\bar{w}^{(5)}_{\max}$ for FCFC nanoplates with $\alpha = 0$ and subjected to $\bar{q} = 1$, using meshes characterized by $n_e = n_x = 40$, and considering diverse Lagrangian elements. See Appendix B for a brief description of the finite elements used in this work. The maximum dimensionless displacement does not change significantly after iteration $i = 5$, consequently, the results in the table refer to iteration 5. Table 3 also considers different values of the slenderness ratio L/t and the length-scale parameter $\lambda_c = L_c/L$. The numerical solution $\bar{w}^{(5)}_{\max}$ is very close to the exact solution $\bar{w}^{\text{exact}}_{\max} = \bar{w}^{\text{exact}}(0.5)$ for all the considered element types. As expected, the higher-order QL9, QL16, and QGLL16 elements exhibit better results than the lower-order Q4 element.

The meshes used for the comparisons reported in Table 3 have the same number of finite elements, $n_e = n_x = 40$, but not the same total number of degrees of freedom. A higher-order finite element has more degrees of freedom than a lower-order element. To enable a fairer assessment of the performance of the different finite elements, the comparisons presented in Table 4 are instead carried out using meshes with the same number of nodes along the x-direction. Specifically, the parameter n_x is set equal to 120, 60, and 40 for nanoplates discretized with Q4, QL9, and QL16 elements, respectively. This ensures that the meshes in Table 4 have the same number of degrees of freedom.

At first glance, the finite elements under consideration appear to exhibit comparable performance, since the dimensionless displacements reported in Table 4 do not differ significantly. To further assess the accuracy of the results, the relative residuals $r^{(5)}_x$ and $r^{(5)}_{zx}$ are reported in Tables 5 and 6 for cases $L/t = 10$ and $L/t = 1000$, respectively, listed in Table 4. These relative residuals are the normalized global residuals $r^{(i)}_x$ and $r^{(i)}_{zx}$ defined in Eq. (38) and evaluated at iteration $i = 5$. The Q4 element yields an error $r^{(5)}_x$

Table 3
Dimensionless displacement $\bar{w}^{(i)}_{\max} = \bar{w}^{(i)}(0.5, \bar{y})$ at iteration $i = 5$ for FCFC nanoplates with $\alpha = 0$, $\bar{q} = 1$, and $n_e = n_x = 40$.

	$10^3\,\bar{w}$					
	$L/t = 10$			$L/t = 1000$		
	$\lambda_c = 0.1$	$\lambda_c = 0.15$	$\lambda_c = 0.2$	$\lambda_c = 0.1$	$\lambda_c = 0.15$	$\lambda_c = 0.2$
Q4	1.666	1.219	0.907	1.474	1.059	0.775
QL9	1.676	1.225	0.911	1.485	1.066	0.779
QL16	1.675	1.225	0.911	1.484	1.066	0.779
QGLL16	1.675	1.225	0.911	1.484	1.066	0.779
$\bar{w}^{\text{exact}}_{\max}$	1.674	1.224	0.910	1.483	1.065	0.778

Table 4
Dimensionless displacement $\bar{w}^{(i)}_{\max} = \bar{w}^{(i)}(0.5, \bar{y})$ at iteration $i = 5$ for FCFC nanoplates with $\alpha = 0$ and $\bar{q} = 1$.

	n_e	$10^3\,\bar{w}$					
		$L/t = 10$			$L/t = 1000$		
		$\lambda_c = 0.1$	$\lambda_c = 0.15$	$\lambda_c = 0.2$	$\lambda_c = 0.1$	$\lambda_c = 0.15$	$\lambda_c = 0.2$
Q4	120	1.6731	1.2238	0.9102	1.4822	1.0644	0.7781
QL9	60	1.6750	1.2248	0.9108	1.4840	1.0655	0.7787
QL16	40	1.6753	1.2250	0.9109	1.4843	1.0656	0.7788
QGLL16	40	1.6753	1.2250	0.9109	1.4843	1.0656	0.7788
$\bar{w}^{\text{exact}}_{\max}$	–	1.6740	1.2244	0.9105	1.4832	1.0651	0.7785

Table 5
Relative residuals $r^{(i)}_x$ and $r^{(i)}_{zx}$ at iteration $i = 5$ for FCFC nanoplates with $\alpha = 0$, $L/t = 10$, and $\bar{q} = 1$ (Note: $a\,e-n$ denotes $a\,10^{-n}$).

Element	n_e	$L/t = 10$					
		$\lambda_c = 0.1$		$\lambda_c = 0.15$		$\lambda_c = 0.2$	
		$r^{(5)}_x$	$r^{(5)}_{zx}$	$r^{(5)}_x$	$r^{(5)}_{zx}$	$r^{(5)}_x$	$r^{(5)}_{zx}$
Q4	120	2e−2	3e−16	2e−2	4e−16	2e−2	4e−16
QL9	60	9e−4	3e−14	8e−4	2e−14	7e−4	1e−14
QL16	40	6e−5	1e−13	4e−5	6e−14	1e−4	1e−13
QGLL16	40	6e−5	6e−14	4e−5	7e−14	1e−4	9e−14

Table 6
Relative residuals $r^{(i)}_x$ and $r^{(i)}_{zx}$ at iteration $i = 5$ for FCFC nanoplates with $\alpha = 0$, $L/t = 1000$, and $\bar{q} = 1$.

Element	n_e	$L/t = 1000$					
		$\lambda_c = 0.1$		$\lambda_c = 0.15$		$\lambda_c = 0.2$	
		$r^{(5)}_x$	$r^{(5)}_{zx}$	$r^{(5)}_x$	$r^{(5)}_{zx}$	$r^{(5)}_x$	$r^{(5)}_{zx}$
Q4	120	2e−2	1e−13	2e−2	7e−14	2e−2	3e−13
QL9	60	9e−4	2e−10	8e−4	1e−10	7e−4	1.0e−10
QL16	40	6e−5	3e−9	4e−5	2e−9	1e−4	2e−9
QGLL16	40	6e−5	2e−9	4e−5	1e−9	1e−4	8e−10

significantly larger than those obtained with the QL9, QL16, and QGLL16 elements, although all these elements produce essentially the same maximum dimensionless displacement.

For the cases examined in Table 4, the maximum dimensionless displacement does not change appreciably beyond the fifth iteration; therefore, the results reported in Table 4 correspond to iteration 5. Nevertheless, the solutions obtained with the proposed FEM-based iterative method should converge to the exact solution as the iteration index i and the number n_e of finite elements in the mesh tend to ∞. Table 7 presents the numerical solutions for increasing values of n_e, thereby appearing to demonstrate the convergence of the method with mesh refinement. The dimensionless displacement $\bar{w}^{(i)}_{\max}$ stabilizes after iteration $i = 5$, as differences with further iterations are observed only beyond the fifth decimal place.

A salient feature of the proposed FEM-based iterative procedure is the dependence of the mesh density on the length-scale parameter λ_c. Here, the mesh density is defined as the number of planar finite elements per unit area. The kernel function ψ, introduced in Section 3.3.2, constitutes a delta sequence, that is, ψ converges to the Dirac delta distribution as $L_c \to 0$

Table 7
Dimensionless displacement $\bar{w}^{(i)}_{\max} = \bar{w}^{(i)}(0.5, \bar{y})$ at iteration $i = 5$ for FCFC nanoplates with $\alpha = 0$, $\bar{q} = 1$, QL16 elements, and considering different levels of mesh refinement.

n_e	$10^3\,\bar{w}$					
	$L/t = 10$			$L/t = 1000$		
	$\lambda_c = 0.1$	$\lambda_c = 0.15$	$\lambda_c = 0.2$	$\lambda_c = 0.1$	$\lambda_c = 0.15$	$\lambda_c = 0.2$
40	1.675 30	1.224 98	0.910 88	1.484 34	1.065 59	0.778 81
60	1.674 58	1.224 66	0.910 70	1.483 72	1.065 31	0.778 65
120	1.674 15	1.224 47	0.910 59	1.483 34	1.065 14	0.778 56
240	1.674 04	1.224 42	0.910 57	1.483 25	1.065 10	0.778 54
$\bar{w}^{\text{exact}}_{\max}$	1.674 00	1.224 38	0.910 49	1.483 22	1.065 07	0.778 46

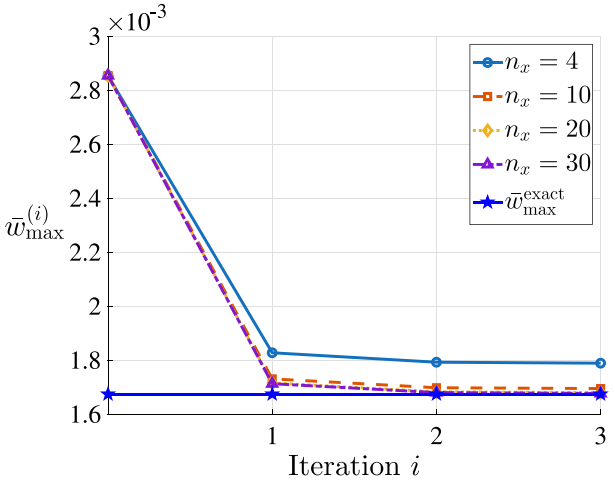

Fig. 6. Dimensionless displacement $\bar{w}^{(i)}_{\max} = \bar{w}^{(i)}(0.5, \bar{y})$ plotted against the iteration index i for different values of the number n_x of finite elements along the x-axis (FCFC nanoplate in cylindrical bending with $\lambda_c = 0.1$, $\alpha = 0$, $L/t = 10$, $\bar{q} = 1$, and QL16 finite elements).

(see Appendix A). As a result, the integrand in Eqs. (23) and (24) may exhibit increasingly sharp variations over the integration domain, corresponding to the mid-plane of the nanoplate.

The integration domain is discretized into $n_x \times n_y$ subdomains, each associated with the area of a finite element. For decreasing values of L_c, an accurate numerical integration requires smaller integration subdomains, namely, finite elements of reduced size. In the one-dimensional setting considered in this section, the finite element size along the x-direction, $a_x = L_x/n_x$, must therefore decrease as the length-scale parameter $\lambda_c = L_c/L$ decreases, implying a monotonically decreasing relationship between λ_c and n_x.

Until now, the calculations have been performed using a relatively large number n_e of finite elements. In view of the delta-like behavior of the kernel function ψ, it is of interest to determine the minimum value of n_e that maintains a satisfactory level of accuracy. In Figs. 6 and 7, $\bar{w}^{(i)}_{\max}$ is plotted versus the iteration index i for several values of n_x. Both figures refer to FCFC nanoplates with $\alpha = 0$, $L/t = 10$, $\bar{q} = 1$, and QL16 elements.

In Fig. 6, corresponding to a length-scale parameter $\lambda_c = 0.1$, the response obtained with the coarsest discretization ($n_x = 4$) differs markedly from that computed with $n_x = 20$, indicating a pronounced sensitivity to mesh refinement. In contrast, the results reported in Fig. 7 for the larger value $\lambda_c = 0.2$ exhibit much smaller discrepancies among the curves corresponding to $n_x = 4, 10, 20$, and 30. This indicates that, for larger λ_c, even relatively coarse meshes provide responses reasonably close to the exact solution. On the basis of the trends observed in Figs. 6 and 7, it may be concluded that selecting $n_x = 2/\lambda_c$ ensures an adequate level of accuracy.

When the mixture ($0 < \alpha < 1$) is adopted in place of the purely nonlocal model ($\alpha = 0$), the proposed iterative method provides a greater level of accuracy. Table 8 reports the maximum dimensionless displacement $\bar{w}^{(10)}_{\max}$ for FCFC nanoplates with $\alpha = 0.5$ and $\bar{q} = 1$. The maximum dimensionless displacement does not change significantly after iteration $i = 5$ in both the purely nonlocal model considered in the previous examples and the local–nonlocal mixture.

Unlike the purely nonlocal model, which shows marginal accuracy gains with further iterations, the local–nonlocal mixture exhibits superior convergence. Within a few steps, the relative residuals reach machine precision in the mixture scheme, as shown in Tables 9 and 10, where the relative residuals $r^{(i)}_x$ and $r^{(i)}_{zx}$ at iteration $i = 10$ are reported for FCFC nanoplates with $\alpha = 0.5$ and $\bar{q} = 1$, also considered in Table 8. Selecting the iteration $i = 10$ serves to illustrate this significant improvement in convergence behavior. The bi-cubic QL16 and QGLL16 elements yield identical results, which are in close agreement with those obtained using the bi-quadratic QL9 element. Given that the error $r^{(10)}_{zx}$ approaches machine precision, the finite element performance is best assessed via the relative residual $r^{(10)}_x$. As shown in Tables 9 and 10, the lower-order Q4 element yields a residual $r^{(10)}_x$ two to three orders of

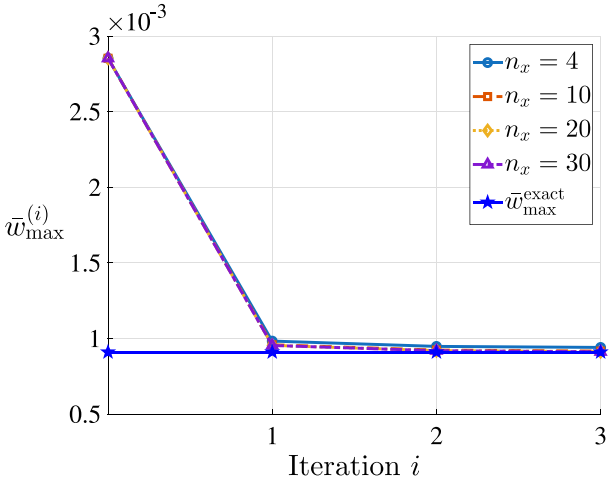

Fig. 7. Dimensionless displacement $\bar{w}^{(i)}_{\max} = \bar{w}^{(i)}(0.5, \bar{y})$ plotted against the iteration index i for different values of the number n_x of finite elements along the x-axis (FCFC nanoplate with $\lambda_c = 0.2$, $\alpha = 0$, $L/t = 10$, and $\bar{q} = 1$, and QL16 finite elements).

Table 8
Dimensionless displacement $\bar{w}^{(i)}_{\max} = \bar{w}^{(i)}(0.5, \bar{y})$ at iteration $i = 10$ for FCFC nanoplates with $\alpha = 0.5$ and $\bar{q} = 1$.

	n_e	$10^3\,\bar{w}$					
		$L/t = 10$			$L/t = 1000$		
		$\lambda_c = 0.1$	$\lambda_c = 0.2$	$\lambda_c = 0.4$	$\lambda_c = 0.1$	$\lambda_c = 0.2$	$\lambda_c = 0.4$
Q4	120	2.2732	1.8939	1.6118	2.0527	1.7029	1.4534
QL9	60	2.2742	1.8945	1.6122	2.0537	1.7035	1.4539
QL16	40	2.2743	1.8946	1.6122	2.0538	1.7035	1.4539
QGLL16	40	2.2743	1.8946	1.6122	2.0538	1.7035	1.4539
$\bar{w}^{\text{exact}}_{\max}$	–	2.2737	1.8944	1.6122	2.0533	1.7034	1.4538

Table 9
Relative residuals $r^{(i)}_x$ and $r^{(i)}_{zx}$ at iteration $i = 10$ for FCFC nanoplates with $\alpha = 0.5$, $L/t = 10$, and $\bar{q} = 1$.

Element	n_e	$L/t = 10$					
		$\lambda_c = 0.1$		$\lambda_c = 0.2$		$\lambda_c = 0.4$	
		$r^{(10)}_x$	$r^{(10)}_{zx}$	$r^{(10)}_x$	$r^{(10)}_{zx}$	$r^{(10)}_x$	$r^{(10)}_{zx}$
Q4	120	6e−6	2e−16	3e−6	2e−16	1e−6	2e−16
QL9	60	3e−7	3e−16	2e−7	2e−16	6e−8	2e−16
QL16	40	2e−8	3e−16	7e−9	3e−16	3e−9	2e−16
QGLL16	40	2e−8	3e−16	7e−9	3e−16	3e−9	3e−16

magnitude higher than those of the QL16 and QGLL16 elements, which achieve the highest precision. Notably, the local–nonlocal mixture model significantly enhances the accuracy of the Q4 element; specifically, the residual $r^{(10)}_x$ for the Q4 element is reduced from 2×10^{-2} in the purely nonlocal model to approximately 3×10^{-6} in the mixture model.

In the case of cylindrical bending, boundary conditions that render the structure statically determinate are easily established. For such structures, the proposed iterative method converges to the exact solution within the first iteration. For instance, the shear-deformable FSFS nanoplates investigated in this work are statically determinate under cylindrical bending, and convergence is achieved immediately; see Caporale et al. (2025) for further details.

6.2. Two-dimensional analyses

In this section, the Poisson's ratio ν is greater than zero (and assumed equal to 0.3), so that bending occurs in both x- and y-directions, and the kernel function (75) is adopted.

In cylindrical bending, highly accurate solutions can be obtained using very fine meshes at a low computational cost, since the number of finite elements is limited to $n_e = n_x$, even in refined analyses. For this reason, determining a sufficiently small value of n_e that ensures an acceptable level of accuracy is of secondary importance in the cylindrical bending case.

Table 10
Relative residuals $r_x^{(i)}$ and $r_{zx}^{(i)}$ at iteration $i = 10$ for FCFC nanoplates with $\alpha = 0.5$, $L/t = 1000$, and $\bar{q} = 1$.

Element	n_e	$L/t = 1000$					
		$\lambda_c = 0.1$		$\lambda_c = 0.2$		$\lambda_c = 0.4$	
		$r_x^{(10)}$	$r_{zx}^{(10)}$	$r_x^{(10)}$	$r_{zx}^{(10)}$	$r_x^{(10)}$	$r_{zx}^{(10)}$
Q4	120	6e−6	2e−16	3e−6	2e−16	1e−6	2e−16
QL9	60	3e−7	5e−14	2e−7	3e−14	6e−8	7e−15
QL16	40	2e−8	1e−12	7e−9	6e−13	3e−9	3e−13
QGLL16	40	2e−8	6e−13	7e−9	2e−13	3e−9	1e−13

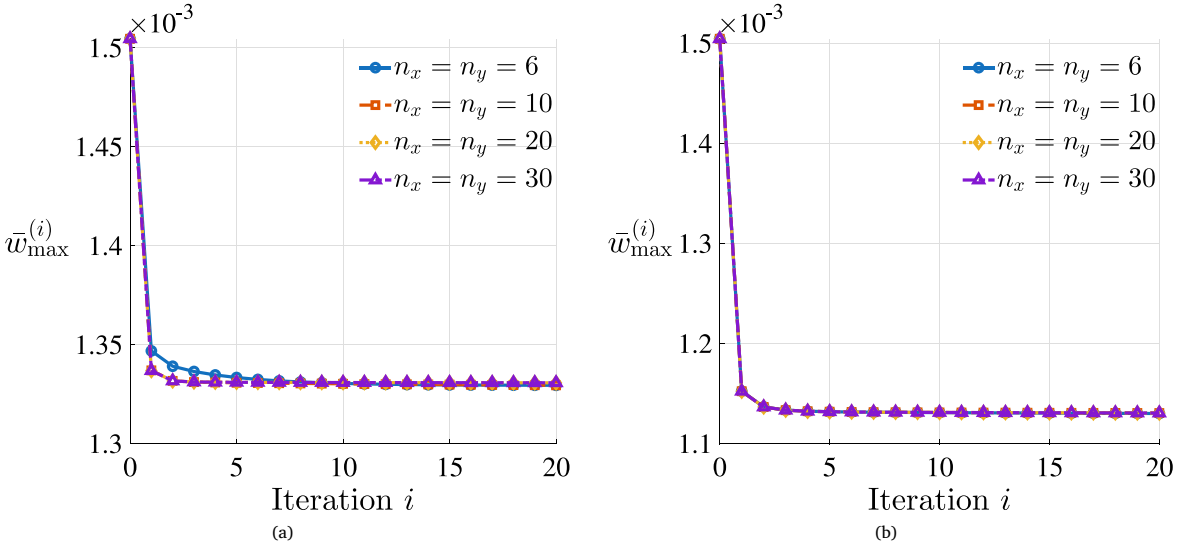

Fig. 8. Dimensionless displacement $\bar{w}_{\max}^{(i)} = \bar{w}^{(i)}(0.5, 0.5)$ plotted against the iteration index i for different mesh densities in CCCC square nanoplate with $\alpha = 0$, $L/t = 10$, $\bar{q} = 1$, and QL16 finite elements. (a) $\lambda_c = 0.05$; (b) $\lambda_c = 0.1$.

By contrast, in two-dimensional analyses, the total number of mesh elements is $n_e = n_x \times n_y$, where n_x and n_y denote the numbers of finite elements along the x- and y-directions, respectively. As a consequence, the mesh size increases rapidly, leading to significantly higher computational costs and motivating the sensitivity analysis presented below, which aims to identify sufficiently small values of n_e that still guarantee an acceptable level of accuracy.

As discussed in Section 6.1, the choice of an appropriate mesh density is governed by the length-scale parameter $\lambda_c = L_c/L$. This dependence persists in the two-dimensional analyses presented in this section. Since the kernel function ψ, introduced in Section 3.3.2, forms a delta sequence, the integrands in Eqs. (23) and (24) may exhibit pronounced spatial variations for smaller values of λ_c. Consequently, a more accurate numerical integration, achieved through mesh refinement, becomes necessary.

Next results are divided into two parts: Section 6.2.1 covers the purely nonlocal model ($\alpha = 0$), while Section 6.2.2 details the local–nonlocal mixture ($0 < \alpha < 1$).

6.2.1. *The purely nonlocal model*

In the cylindrical bending discussed in Section 6.1, the solution stabilized after the fifth iteration for the purely nonlocal model. Hence, it can be said that the solution's accuracy depends solely on the model's degrees of freedom, that is, the number and order of the finite elements in the mesh. When the nanoplate bends in two directions, a more complex behavior occurs, requiring more iterations to satisfy the criterion in Eq. (37). This is particularly true for large values of the length-scale parameter λ_c and for SSSS BCs.

The effect of mesh refinement on the convergence of $\bar{w}^{(i)}$ as $i \to \infty$ is illustrated in Fig. 8, where the maximum dimensionless displacement $\bar{w}_{\max}^{(i)}$ is plotted against the iteration index i for different element sizes, obtained by varying the product $n_x \times n_y$. The figure refers to the CCCC square nanoplate with $\alpha = 0$, $L/t = 10$, $\bar{q} = 1$, and QL16 finite elements. The dimensionless displacement $\bar{w}_{\max}^{(i)}$ is given by $\bar{w}^{(i)}$ evaluated at the center point $(\bar{x}, \bar{y}) = (0.5, 0.5)$ of the mid-plane of the nanoplate. In Fig. 8(a), corresponding to $\lambda_c = 0.05$, the piecewise linear curve obtained with $n_x = n_y = 6, 10$ deviates from that obtained with $n_x = n_y = 20, 30$, indicating a mesh sensitivity for this length-scale parameter. By contrast, in Fig. 8(b), computed with the larger value $\lambda_c = 0.1$, the curves are nearly coincident, showing that very coarse meshes characterized by $n_x = n_y = 6, 10$ provide an accuracy comparable to that of finer meshes with $n_x = n_y = 20, 30$.

Table 11
Dimensionless displacement $\bar{w}^{(i)}_{\max} = \bar{w}^{(i)}(0.5, 0.5)$ at iteration $i = 5$ for $\lambda_c = 0.05$, and iteration $i = 10$ for $\lambda_c = 0.1$, in CCCC square nanoplates with $\alpha = 0$, $L/t = 10$, and $\bar{q} = 1$.

		$10^3\ \bar{w}$	
		$L/t = 10$	
		$\lambda_c = 0.05$	$\lambda_c = 0.1$
Q4	$n_x = n_y = 120$ for $\lambda_c = 0.05$ $n_x = n_y = 60$ for $\lambda_c = 0.10$	1.330 08	1.126 38
QL9	$n_x = n_y = 60$ for $\lambda_c = 0.05$ $n_x = n_y = 30$ for $\lambda_c = 0.10$	1.331 05	1.131 24
QL16	$n_x = n_y = 40$ for $\lambda_c = 0.05$ $n_x = n_y = 20$ for $\lambda_c = 0.10$	1.331 06	1.131 28
QGLL16	$n_x = n_y = 40$ for $\lambda_c = 0.05$ $n_x = n_y = 20$ for $\lambda_c = 0.10$	1.331 06	1.131 28
QL16-FI	$n_x = n_y = 40$ for $\lambda_c = 0.05$ $n_x = n_y = 20$ for $\lambda_c = 0.10$	1.331 06	1.131 28

Table 12
Relative residuals $r^{(i)}_x$, $r^{(i)}_{xy}$, and $r^{(i)}_{zx}$ at iteration $i = 5, 10$ for CCCC square nanoplates with $\alpha = 0$, $L/t = 10$, and $\bar{q} = 1$.

Element	n_e	$L/t = 10$					
		$\lambda_c = 0.05$			$\lambda_c = 0.10$		
		$r^{(5)}_x$	$r^{(5)}_{xy}$	$r^{(5)}_{zx}$	$r^{(10)}_x$	$r^{(10)}_{xy}$	$r^{(10)}_{zx}$
Q4	$n_x = n_y = 120$ for $\lambda_c = 0.05$ $n_x = n_y = 60$ for $\lambda_c = 0.10$	2e−2	8e−3	3e−3	3e−2	2e−2	7e−3
QL9	$n_x = n_y = 60$ for $\lambda_c = 0.05$ $n_x = n_y = 30$ for $\lambda_c = 0.10$	2e−3	2e−3	3e−3	5e−3	6e−3	7e−3
QL16	$n_x = n_y = 40$ for $\lambda_c = 0.05$ $n_x = n_y = 20$ for $\lambda_c = 0.10$	9e−4	2e−3	3e−3	2e−3	6e−3	6e−3
QGLL16	$n_x = n_y = 40$ for $\lambda_c = 0.05$ $n_x = n_y = 20$ for $\lambda_c = 0.10$	9e−4	2e−3	3e−3	2e−3	6e−3	6e−3
QL16-FI	$n_x = n_y = 40$ for $\lambda_c = 0.05$ $n_x = n_y = 20$ for $\lambda_c = 0.10$	9e−4	2e−3	3e−3	2e−3	6e−3	7e−3

It is worth noting that the local solution, corresponding to classical elasticity, is given by $\bar{w}^{(0)}$, i.e., the dimensionless displacement $\bar{w}$ at the initial iteration $i = 0$. This local solution is independent of the adopted finite element mesh. By contrast, the nonlocal approximations $\bar{w}^{(i)}$ for $i > 0$ exhibit a dependence on the mesh resolution when $\lambda_c = 0.05$.

Table 11 reports the dimensionless displacement $\bar{w}^{(i)}_{\max} = \bar{w}^{(i)}(0.5, 0.5)$ for CCCC square nanoplates with $\alpha = 0$, $L/t = 10$, and $\bar{q} = 1$. The values in the table refer to the iteration $i = 5$ for $\lambda_c = 0.05$ and iteration $i = 10$ for $\lambda_c = 0.1$. The considered meshes have different numbers of finite elements, but the same number of nodes and degrees of freedom. Fig. 8(a) has shown that twenty QL16 finite elements per direction are sufficient to obtain accurate results for $\lambda_c = 0.05$. Therefore, the forty elements per direction adopted in Table 11 ensure that the results are mesh-independent. Similar observations apply to the case $\lambda_c = 0.1$.

Table 12 lists the relative residuals $r^{(i)}_x$, $r^{(i)}_{xy}$, and $r^{(i)}_{zx}$ for the same cases considered in Table 11. These residuals are larger than those observed for the cylindrical bending case in Section 6.1. This discrepancy is further amplified as the length-scale parameter λ_c increases or when boundary conditions other than CCCC are imposed.

To further investigate this aspect, in Fig. 9 the dimensionless displacement $\bar{w}^{(i)}_{\max}$ is plotted against the iteration index i for the SSSS square nanoplate with $\lambda_c = 0.1$, $\alpha = 0$, $L/t = 10$, $\bar{q} = 1$, and discretized with QL16 elements. The figure shows that the displacement does not converge even after many iterations and continues to decrease.

In Fig. 10, the relative residuals $r^{(i)}_x$, $r^{(i)}_{xy}$, and $r^{(i)}_{zx}$ are plotted against the iteration index for the same nanoplate considered in Fig. 9 with $n_x = n_y = 30$. Even after several dozen iterations, the relative residuals remain high: $r^{(i)}_{zx}$ at iteration $i = 40$ exceeds 2%.

This behavior becomes dramatically more pronounced as λ_c increases, and for certain boundary conditions.

The origin of this pathological behavior is illustrated in Fig. 11, referring to the same nanoplate of Fig. 9 with $n_x = n_y = 20$. In the following, a bar over a symbol denotes its dimensionless counterpart; for example, $\bar{\chi}_x = \chi_x L$, where χ_x is a dimensional curvature. Fig. 11(a) shows the dimensionless local curvature $\Delta\bar{\chi}^{\mathrm{lc}(i-1)}_x$ when the iteration index i is equal to 40. The relevant dimensionless nonlocal curvature is $\Delta\bar{\chi}^{\mathrm{nl}(i)}_x = \psi * \Delta\bar{\chi}^{\mathrm{lc}(i-1)}_x$ and is illustrated in Fig. 11(b). First, it is observed that the dimensionless local curvature is several orders of magnitude greater than its nonlocal counterpart. Consequently, the residual to be imposed in the subsequent iteration, defined as $\bar{\chi}^{\mathrm{res}(i)}_x = \Delta\bar{\chi}^{\mathrm{nl}(i)}_x - \Delta\bar{\chi}^{\mathrm{lc}(i-1)}_x$, is significantly large in absolute value. Furthermore, pronounced boundary effects emerge, stemming from the convolution integral utilized to evaluate $\Delta\bar{\chi}^{\mathrm{nl}(i)}_x$. The curvature distributions depicted in Fig. 11 for $i = 40$

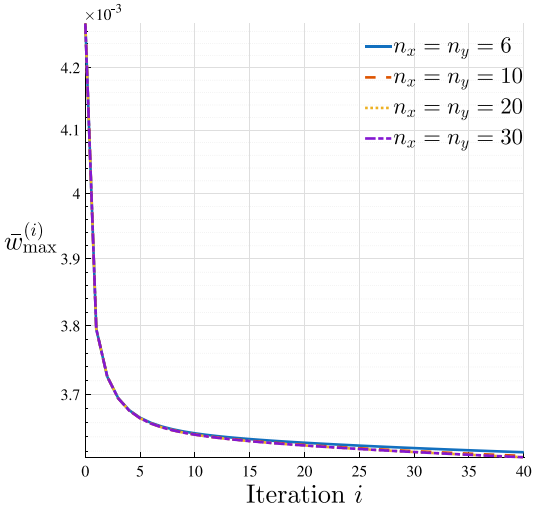

Fig. 9. Dimensionless displacement $\bar{w}^{(i)}_{\max} = \bar{w}^{(i)}(0.5, 0.5)$ plotted against the iteration index i for different mesh densities in the SSSS square nanoplate with $\lambda_c = 0.1$, $\alpha = 0$, $L/t = 10$, $\bar{q} = 1$, and QL16 finite elements.

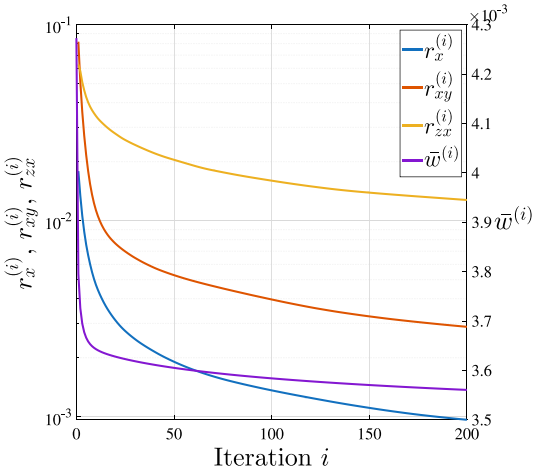

Fig. 10. Relative residuals plotted against the iteration index i for the SSSS square nanoplate with $\lambda_c = 0.1$, $\alpha = 0$, $L/t = 10$, $\bar{q} = 1$, and QL16 finite elements ($n_x = n_y = 30$).

do not depend on the mesh density, for meshes not coarser than the adopted one characterized by $n_x = n_y = 20$, and are replicated almost identically in subsequent iterations ($i > 40$). This leads to persistent looping behavior, in which convergence, if achieved at all, proceeds at an extremely slow rate.

These observations motivate the need for an alternative modeling approach. The subsequent local–nonlocal mixture effectively resolves this convergence issue.

Before addressing the local–nonlocal mixture, it is worth noting, from Fig. 10, that acceptable solutions could be obtained if the relative residuals $r_{xy}^{(i)}$ and $r_{zx}^{(i)}$ were not taken into account. This situation arises, for instance, in Kirchhoff nanoplates (where the residuals $r_{zx}^{(i)}$ and $r_{zy}^{(i)}$ are inherently equal to zero), under the assumption that the nonlocal constitutive law acts only on the curvatures χ_x^{el} and χ_y^{el}, so that the residual $r_{xy}^{(i)}$ results equal to zero, as done in Farajpour et al. (2020). In Fig. 12, the ratio $w_{\max}/w_{\max}^{(0)}$ is plotted against L_c/L_x for the SSSS square nanoplate with $\alpha = 0$, $L/t = 1000$, and $\bar{q} = 1$. Here, $w_{\max}$ and $w_{\max}^{(0)}$ are the nonlocal and local displacements, respectively, evaluated at the center point $(\bar{x}, \bar{y}) = (0.5, 0.5)$ of the nanoplate. The blue circles of Fig. 12 are obtained with the FEM-based iterative method presented in the previous sections, adopting a mesh with QL16 elements ($n_x = n_y = 100$), the convolution kernel of Farajpour et al. (2020), and assuming that the nonlocal constitutive law only holds for χ_x^{el} and χ_y^{el}. Under this assumption, all relative residuals vanish except for $r_x^{(i)}$ and $r_y^{(i)}$. For the blue circles, $w_{\max}$ is the displacement $w_{\max}^{(i)}$ evaluated at the iteration index $i = 100$ and the corresponding residual $r_{\max}$ is equal to 0.004 (see the end of Section 6.2.2 for the definition of $r_{\max}$). The black curve of Fig. 12 is from Farajpour et al. (2020), where the original integral formulation of the stress-driven nonlocal problem has been transformed into an equivalent differential form represented by a differential equation accompanied by

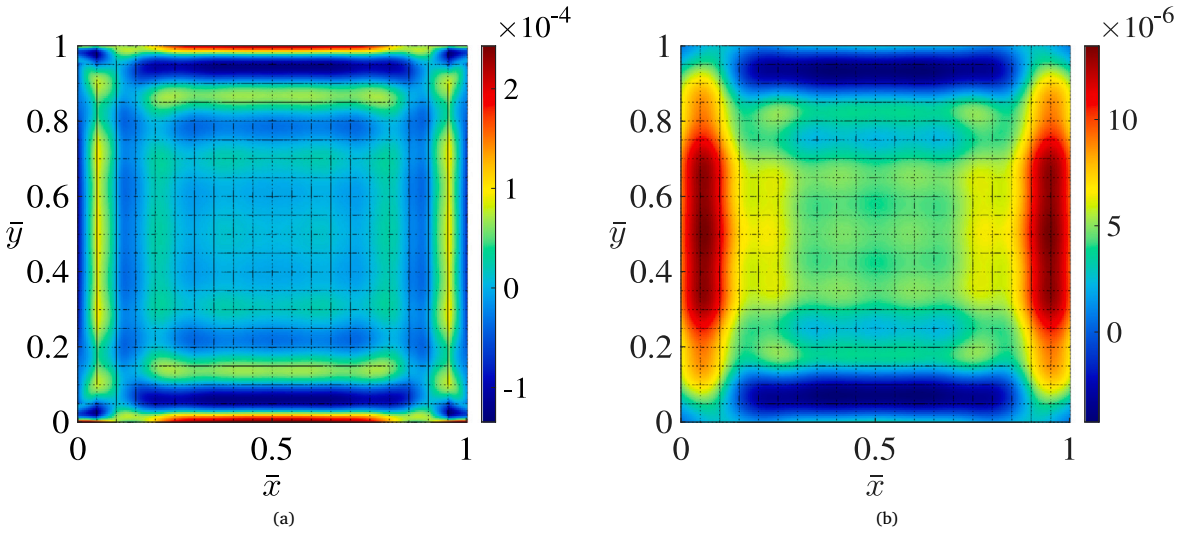

Fig. 11. Dimensionless curvatures in SSSS square nanoplate with $\lambda_c = 0.1$, $\alpha = 0$, $L/t = 10$, $\bar{q} = 1$, QL16 elements ($n_x = n_y = 20$). (a) Dimensionless local curvature $\Delta\bar{\chi}_x^{\mathrm{lc}(i-1)}$ when the iteration index i is equal to 40. (b) The relevant dimensionless nonlocal curvature $\Delta\bar{\chi}_x^{\mathrm{nl}(i)} = \psi * \Delta\bar{\chi}_x^{\mathrm{lc}(i-1)}$ with $i = 40$.

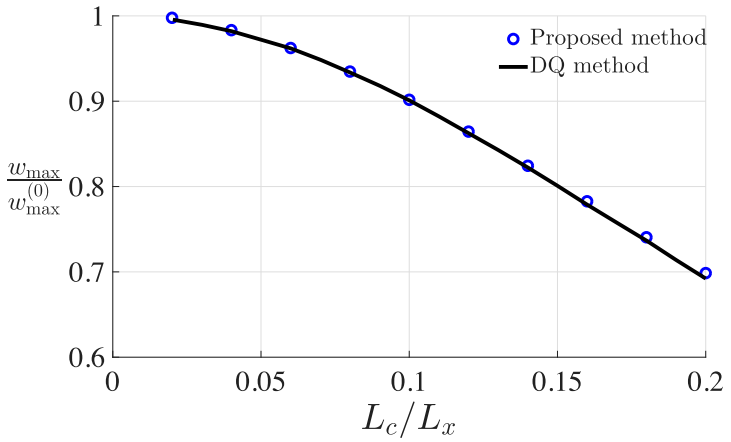

Fig. 12. The ratio $w_{\max}/w_{\max}^{(0)}$ plotted against L_c/L_x for SSSS square nanoplates with $\alpha = 0$, $L/t = 1000$, $\bar{q} = 1$.

the constitutive boundary conditions. The problem has then been solved in its differential form using the differential quadrature (DQ) technique. The comparison in Fig. 12 demonstrates a good agreement between the two sets of results, despite being obtained with very different methods, both in terms of theoretical formulation and computational strategy. It is worth emphasizing that deriving a differential formulation from the integral form of a nonlocal problem is nontrivial and typically requires restrictive assumptions. In Farajpour et al. (2020), for instance, a rectangular plate geometry and a specific convolution kernel are assumed. In contrast, the iterative approach presented here is more general and can be applied to nanoplates of arbitrary geometry and kernel functions.

6.2.2. *The local–nonlocal mixture*

The amount of local and nonlocal elastic phases in the mixture model is governed by the parameter α. The purely nonlocal model is obtained by setting $\alpha = 0$, whereas values of α in the open interval $(0, 1)$ provide a mixture. Therefore, as the parameter α decreases, the response increasingly approaches that of the purely nonlocal model, which is known to exhibit convergence difficulties. For this reason, although α has a physical meaning related to the constitutive law, it also plays a computational role. Increasing α shifts the behavior away from that of the purely nonlocal model and significantly improves the convergence rate. Nevertheless, even small values of α ensure convergence, albeit at the cost of a larger number of iterations—a property that is not guaranteed in the purely nonlocal formulation.

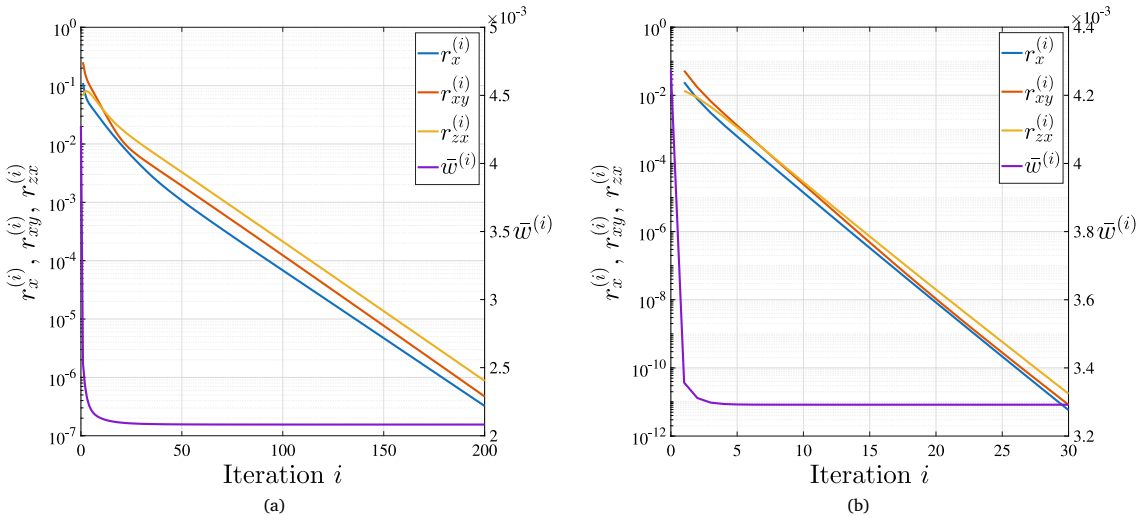

Fig. 13. Relative residuals plotted against the iteration index i for the SSSS square nanoplate with $\lambda_c = 0.3$, $L/t = 10$, $\bar{q} = 1$, and QL16 finite elements ($n_x = n_y = 10$). (a) $\alpha = 0.05$. (b) $\alpha = 0.5$.

This aspect of the convergence is shown in Fig. 13, where the relative residuals are plotted against the iteration index i for the SSSS square nanoplate with $\lambda_c = 0.3$, $L/t = 10$, $\bar{q} = 1$, and QL16 finite elements. Fig. 13(a) shows the residuals obtained for a small value of the mixing parameter, $\alpha = 0.05$, whereas Fig. 13(b) reports the corresponding residuals for a moderate value, $\alpha = 0.5$.

Fig. 13 employs two different vertical scales in order to present all relevant quantities within a single panel. The left vertical axis, on a logarithmic scale, corresponds to the relative residuals, while the right vertical axis, on a linear scale, corresponds to the dimensionless displacement $\bar{w}^{(i)}$. The horizontal grid lines are drawn according to the logarithmic scale of the left axis and are intended solely to facilitate the interpretation of the residual curves. They do not represent metric reference levels for the quantity associated with the right vertical axis.

Fig. 13 illustrates the linear convergence behavior of the iterative scheme, further substantiating the aforementioned observations. It is evident that the rate of convergence is highly sensitive to the choice of the mixing parameter α; specifically, the process exhibits slow convergence for small values (e.g., $\alpha = 0.05$), whereas more moderate values (e.g., $\alpha = 0.5$) significantly accelerate the error reduction.

The considered finite elements, with the adopted selective quadrature scheme, avoid shear locking in thin nanoplates. Thus, the proposed iterative method can also be adopted for thin nanoplates. In Fig. 14, the relative residuals are plotted against the iteration index i for the thin square nanoplate with SSSS boundary conditions, $\lambda_c = 0.3$, $L/t = 1000$, $\bar{q} = 1$, and QL16 finite elements. For the thin nanoplate considered in Fig. 14, the rate of convergence has similar trends to that of the moderately thick nanoplate of Fig. 13.

To further investigate the influence of the mixing parameter α on the convergence rate, Fig. 15 reports the smallest iteration index i for which the residual $r^{(i)}$, defined in Eq. (37), becomes less than the prescribed tolerance $tol = 0.001$. The results are plotted as functions of the mixing parameter $\alpha \in [0.02, 1]$ for square nanoplates with $\lambda_c = 0.1$, $L/t = 10$, $\bar{q} = 1$, and a QL16 finite-element discretization with $n_x = n_y = 20$.

The figure shows that the prescribed tolerance is achieved after only a few iterations for most values of α. However, the number of iterations required for convergence increases rapidly as α decreases below 0.1. Nanoplates with SSSS boundary conditions require a larger number of iterations to achieve convergence than CCCC nanoplates. For even smaller values of α, e.g., $\alpha = 0.0001$, the purely nonlocal model and the local–nonlocal mixture model not only yield practically identical displacement fields, but also exhibit similar convergence behavior, namely, about the same number of iterations required to attain a prescribed tolerance.

The mixing parameter α also plays a physical role. The nonlocal part of the mixture involves a stiffening effect. Consequently, decreasing α increases the weight of the nonlocal term and leads to a reduction in the displacement of the nanostructures. For moderate values of α, the resulting nanoplates are therefore softer than their purely nonlocal counterparts. To counteract this softening behavior, larger values of the length-scale parameter λ_c must be adopted. The monotonically decreasing relationship between λ_c and the mesh density (represented by $n_x \times n_y$) also applies to the mixture model. Accordingly, larger values of λ_c permit the use of coarser finite element discretizations, yielding a substantial computational advantage. In Figs. 13 and 14, a very coarse mesh constituted of $n_x \times n_y = 10 \times 10$ finite elements is adopted for the residuals corresponding to a large parameter λ_c.

In this section, it is also of interest to assess solutions obtained with different types of finite elements and to compare their corresponding relative residuals. Table 13 reports the maximum dimensionless displacement $\bar{w}^{(i)}_{\max} = \bar{w}^{(i)}(0.5, 0.5)$ for SSSS square nanoplates with $\lambda_c = 0.3$, $\alpha = 0.5$, and $\bar{q} = 1$. The table considers both moderately thick ($L/t = 10$) and thin ($L/t = 1000$) nanoplates

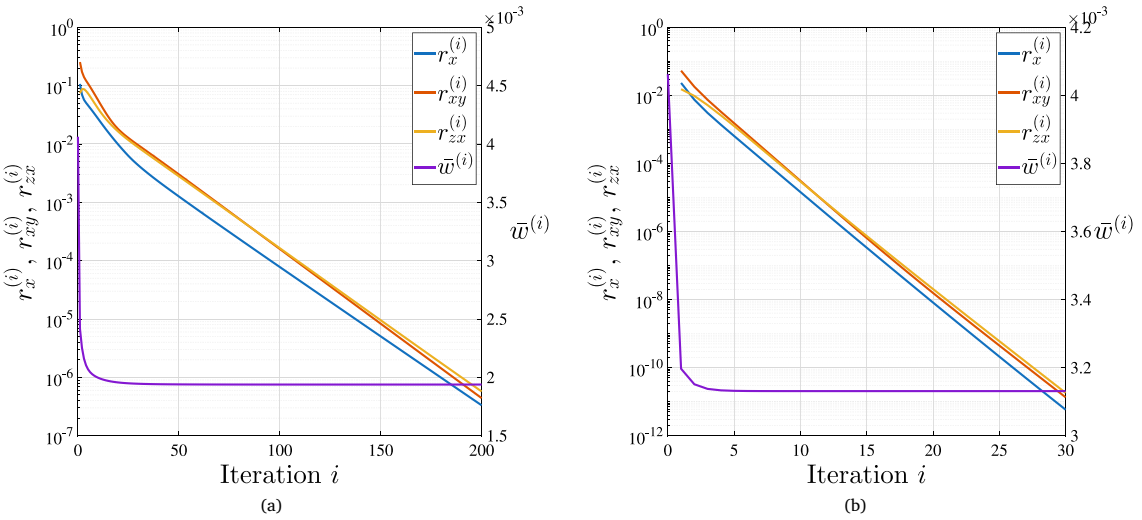

Fig. 14. Relative residuals plotted against the iteration index i for the SSSS square nanoplate with $\lambda_c = 0.3$, $L/t = 1000$, $\bar{q} = 1$, and QL16 finite elements ($n_x = n_y = 10$). (a) $\alpha = 0.05$. (b) $\alpha = 0.5$.

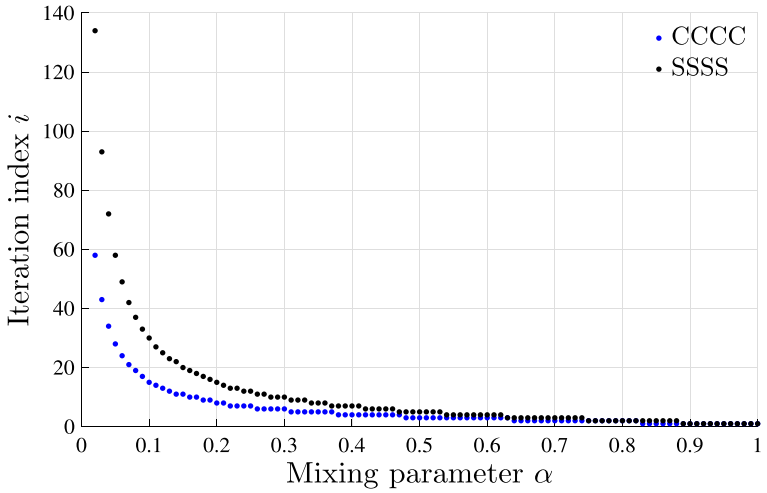

Fig. 15. The iteration i at which the residual $r^{(i)}$, as defined in Eq. (37), becomes less than the tolerance $tol = 0.001$ for $\alpha \in [0.02, 1]$ in square nanoplates with $\lambda_c = 0.1$, $L/t = 10$, $\bar{q} = 1$, QL16 finite element ($n_x = n_y = 20$).

discretized with different finite elements. The meshes have the same number of nodes and total degrees of freedom. Table 14 reports the relative residuals corresponding to the cases of Table 13. These residuals are already small at the relatively low iteration count $i = 15$. Notably, the different finite element types yield identical residuals. In contrast, for the purely nonlocal model, the Q4 element exhibits substantially larger residuals than those of the higher-order elements QL9, QL16, and QGLL16. This further confirms the robustness and effectiveness of the mixture model.

In Fig. 16, the ratio $w_{\max}^{(i)}/w_{\max}^{(0)}$ is plotted against L_c/L_x for CCCC square nanoplates with $L/t = 10$, $\bar{q} = 1$, and QL16 finite elements. $w_{\max}^{(i)}$ and $w_{\max}^{(0)}$ are the nonlocal and local displacements, respectively, evaluated at the center point $(\bar{x}, \bar{y}) = (0.5, 0.5)$ of the nanoplates. The figure also reports the iteration index i at which the nonlocal displacement $w_{\max}^{(i)}$ is attained, together with the corresponding residual $r_{\max}$. Recalling that $r^{(i)}$ denotes the relative residual defined in Eq. (37) and evaluated at the iteration i of the solution process for a given value of the parameter $\lambda_c = L_c/L_x$, the quantity $r_{\max}$ is defined as the maximum among all such residuals associated with the computation of the points of a single curve in Fig. 16, where i is the last iteration of the process. Specifically,

$$r_{\max} = \max\left\{ r^{(i)} \;\middle|\; \lambda_c = 0.02, 0.04, 0.06, \ldots, 1 \right\}. \tag{71}$$

Table 13
Dimensionless displacement $\bar{w}^{(i)}_{\max} = \bar{w}^{(i)}(0.5, 0.5)$ at iteration $i = 15$ for SSSS square nanoplates with $\lambda_c = 0.3$, $\alpha = 0.5$, and $\bar{q} = 1$.

		$10^3\,\bar{w}$	
		$L/t = 10$	$L/t = 1000$
Q4	$n_x = n_y = 30$	3.290 492	3.129 183
QL9	$n_x = n_y = 15$	3.292 015	3.131 079
QL16	$n_x = n_y = 10$	3.292 012	3.131 077
QGLL16	$n_x = n_y = 10$	3.292 012	3.131 077
QL16-FI	$n_x = n_y = 10$	3.292 011	3.131 131

Table 14
Relative residuals $r^{(i)}_x$, $r^{(i)}_{xy}$, and $r^{(i)}_{zx}$ at iteration $i = 15$ for SSSS square nanoplates with $\lambda_c = 0.3$, $\alpha = 0.5$, and $\bar{q} = 1$.

Element	n_e	$L/t = 10$			$L/t = 1000$		
		$r^{(15)}_x$	$r^{(15)}_{xy}$	$r^{(15)}_{zx}$	$r^{(15)}_x$	$r^{(15)}_{xy}$	$r^{(15)}_{zx}$
Q4	$n_x = n_y = 30$	4e−7	6e−7	7e−7	4e−7	7e−7	7e−7
QL9	$n_x = n_y = 15$	3e−7	5e−7	8e−7	3e−7	6e−7	7e−7
QL16	$n_x = n_y = 10$	3e−7	5e−7	7e−7	3e−7	6e−7	7e−7
QGLL16	$n_x = n_y = 10$	3e−7	5e−7	7e−7	3e−7	6e−7	7e−7
QL16-FI	$n_x = n_y = 10$	3e−7	5e−7	7e−7	3e−7	6e−7	1e−6

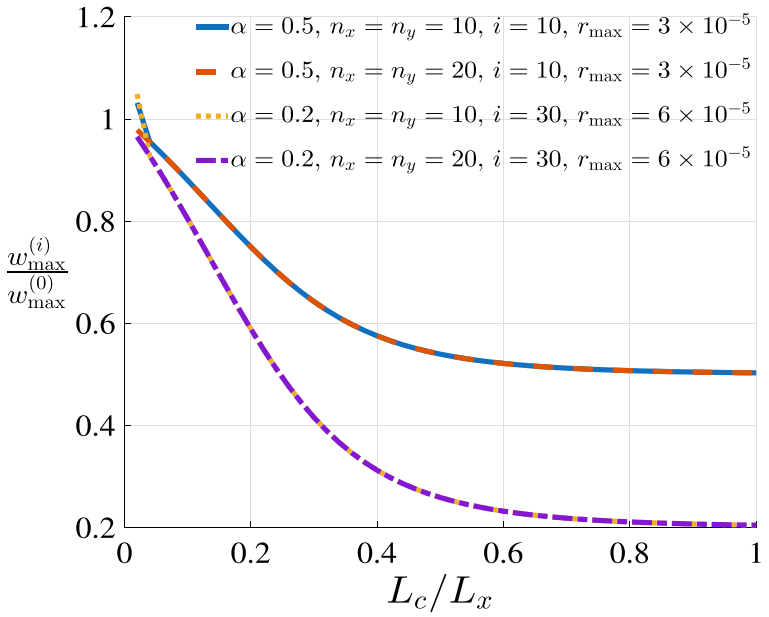

Fig. 16. The ratio $w^{(i)}_{\max}/w^{(0)}_{\max}$ plotted against L_c/L_x for CCCC square nanoplates with $L/t = 10$, $\bar{q} = 1$, and QL16 finite elements.

For a fixed value of α, the nonlocal displacement decreases as the parameter λ_c increases, indicating a monotonic reduction in displacement. For a fixed λ_c, decreasing α also leads to a decrease in the nonlocal displacement. Both trends are attributable to the stiffening effect introduced by the nonlocal component of the mixture. For a given value of α, two curves are shown, corresponding to mesh densities $n_x = n_y = 10$ and $n_x = n_y = 20$. The coincidence of these curves for fixed α indicates that the coarse mesh with $n_x = n_y = 10$ provides accurate results even for relatively small values of λ_c. This agreement holds down to $\lambda_c = 0.04$. For smaller values of λ_c, the curves begin to diverge, signaling the need for increased mesh refinement. Similar trends are observed for the SSSS square nanoplates, as illustrated in Fig. 17.

Figs. 16 and 17 exhibit a stiffening behavior, namely, the maximum displacement decreases as the dimensionless length-scale parameter λ_c increases. This trend is consistent with the experimental evidence reported in Lam et al. (2003), where several cantilever microbeams made of the same material and having the same length-to-thickness ratio $L/t = 10$ were tested in bending. As shown, for instance, in Fig. 12 of Lam et al. (2003), the maximum displacement $w_{\max}$ decreases as the beam size decreases, in contrast with classical bending theory, according to which beams with the same L/t exhibit the same $w_{\max}$. In the present nonlocal

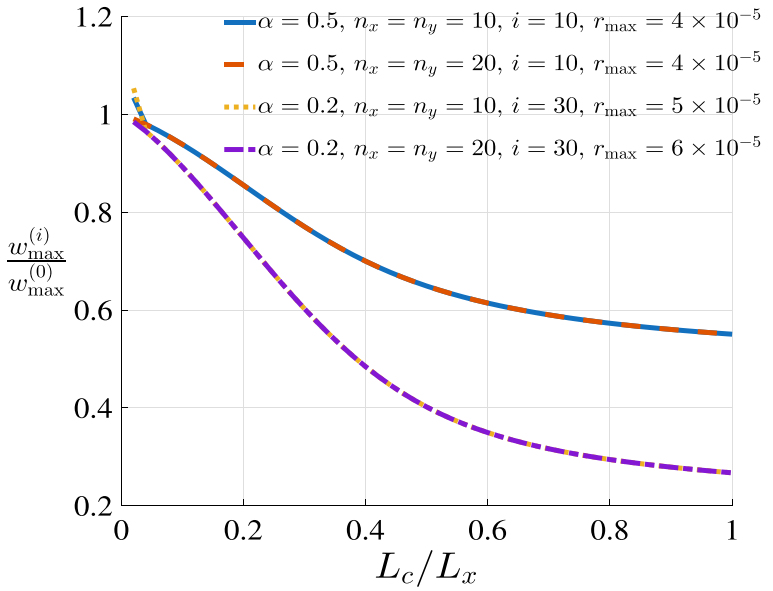

Fig. 17. The ratio $w_{\max}^{(i)}/w_{\max}^{(0)}$ plotted against L_c/L_x for SSSS square nanoplates with $L/t = 10$, $\bar{q} = 1$, and QL16 finite elements.

framework, $\lambda_c = L_c/L$ is a size-dependent parameter: for a given material, L_c remains constant, whereas λ_c increases as the beam length L decreases. Hence, the displacement decreases as the structure size decreases, or equivalently as λ_c increases.

However, the sole parameter λ_c is not sufficient to capture the full experimental response. For this reason, the local–nonlocal model introduces an additional parameter, α, to improve the fitting of the experimental data. The calibration of the model parameters λ_c and α is based on the following observations.

Setting

$$w^* = w_{\max}^{(i)}/w_{\max}^{(0)}, \tag{72}$$

the curves $w^* = w^*(\lambda_c)$ in Figs. 16 and 17 satisfy $w^* = 1$ at $\lambda_c = 0$, and their curvature $d^2w^*/d\lambda_c^2$ changes from negative to positive as λ_c increases from 0 to 1. Therefore, λ_c controls the overall shape of the curves, namely whether the graph of $w^* = w^*(\lambda_c)$ does or does not undergo a change in the sign of $d^2w^*/d\lambda_c^2$. By contrast, the mixture parameter α measures the amount by which w^* decreases for a given increase in λ_c. For example, Fig. 17 suggests that the inflection point, i.e., the point where $d^2w^*/d\lambda_c^2$ changes sign, occurs approximately at $\lambda_c \approx 0.3$, and this behavior is observed for several values of α. Suppose that an experimental curve of w^* versus the reciprocal x_{d} of the structure size is available, for instance with $x_{\mathrm{d}} = 1/L$. The experiments are performed on samples made of the same material: L_c is an unknown but fixed constant. Then, the condition $\lambda_c = 0.3$ at the point where

$$\frac{d^2w^*}{dx_{\mathrm{d}}^2} = 0 \tag{73}$$

provides an estimate of the length-scale parameter L_c. Once L_c has been determined, the experimental values of w^* can be replotted as functions of $\lambda_c = L_c/L$, and the parameter α can then be calibrated by fitting the experimental and numerical curves $w^* = w^*(\lambda_c)$. In fact, the experimental and numerical curves already coincide at the point $\lambda_c = 0$. Imposing their coincidence at an additional point, for instance at $\lambda_c = 0.3$, allows the parameter α to be determined. This represents one possible strategy for calibrating the model parameters, whereas alternative procedures may be adopted depending on the specific trends exhibited by the experimental data.

Although the proposed model captures the stiffening behavior observed experimentally, a nonlocal model capable of reproducing also a softening behavior with increasing λ_c would be desirable. Such a model can be obtained by incorporating a stress-gradient contribution into the nonlocal constitutive laws introduced in Section 3.3.2; see also Barretta and Marotti de Sciarra (2019) for stress-gradient formulations in one-dimensional problems.

7. Concluding remarks

Eringen's nonlocal elasticity in integral form (Eringen, 1972, 1983) has generated hundreds of works, in which nonlocal problems were solved by considering a differential form deemed equivalent to the integral form. For nonlocal beams, Romano et al. (2017) demonstrated that the integral and differential formulations are equivalent if constitutive boundary conditions are introduced into the differential form. An analogous result was found for nonlocal plates by Farajpour et al. (2020). Unfortunately, deriving a differential formulation from the integral form of a nonlocal problem is nontrivial for two-dimensional structures and typically

requires restrictive assumptions. To the best of the authors' knowledge, only Farajpour et al. (2020) have derived a consistent differential formulation (i.e., equipped with constitutive boundary conditions) from the integral form for two-dimensional nonlocal structures. Therefore, alternative approaches are needed to address problems involving two-dimensional structures, such as nonlocal plates. To this end, a novel iterative approach is applied to solve the nonlocal plate problem, with nonlocality expressed in integral form in a stress-driven approach.

Specifically, a FEM-based iterative strategy is developed for the elastostatic analysis of shear-deformable nanoplates. Size-dependent effects are incorporated through a two-phase local–nonlocal constitutive model, in which the nonlocal contribution is evaluated in a stress-driven manner via an integral convolution of the stress resultants. Several numerical applications are presented to assess the performance of the proposed approach in two distinct regimes.

First, the purely nonlocal case — obtained by suppressing the local phase of the two-phase model — is investigated. For this formulation, it is observed that, under certain boundary conditions and for large values of the length-scale parameter λ_c, the relative residual remains significant even after many iterations, casting doubt on the iterative scheme's convergence.

Conversely, when the local phase is retained within the mixture, the aforementioned convergence issues are completely eliminated, and a robust numerical behavior is recovered. The iterative scheme exhibits rapid and stable convergence, with a fast linear rate for balanced local–nonlocal mixtures and a slower, yet still linear, convergence for nonlocal-dominated mixtures with a small local fraction. Moreover, accurate solutions are obtained even with very coarse meshes for small values of the length-scale parameter, namely $\lambda_c = 0.02$–0.04.

It is worth emphasizing that, although the proposed formulation is developed within a shear-deformable framework, the iterative strategy combined with the local–nonlocal mixture model exhibits robust and stable convergence for both moderately thick and thin nanoplates. This is a noteworthy result, as thin-plate formulations are well known to be prone to numerical instabilities and convergence difficulties. The presence of the local phase within the mixture effectively regularizes the problem, ensuring stable numerical behavior independently of the plate thickness.

Owing to its robustness and flexibility, the proposed formulation is applicable to arbitrary geometries, kernel functions, and general boundary and loading conditions. As such, it provides an effective and reliable computational framework for the analysis and design of a broad class of nanostructured plate systems of current interest in Nano-Engineering.

CRediT authorship contribution statement

Andrea Caporale: Writing – review & editing, Writing – original draft, Validation, Software, Methodology, Conceptualization. **Marzia Sara Vaccaro:** Writing – review & editing, Writing – original draft, Validation, Software, Conceptualization. **Raffaele Barretta:** Writing – review & editing, Writing – original draft, Validation, Software, Conceptualization. **Raimondo Luciano:** Writing – review & editing, Writing – original draft, Validation, Software, Conceptualization.

Declaration of competing interest

The authors declare that they have no known competing financial interests or personal relationships that could have appeared to influence the work reported in this paper.

Acknowledgments

The research leading to these results has received funding from Project "P20223PLC2 - Nonlocal modelling of nano-coatings (NanoCo)" CUP H53D23008500001 funded by European Union in NextGenerationEU plan, Mission 4, Component 2, Investment 1.1 through the Italian "Bando Prin 2022 PNRR - D.D. 1409 of September 14, 2022" by MUR.

Appendix A. Kernels adopted in Section 6

For the cylindrical bending of nanoplates investigated in Section 6.1, the following one-dimensional kernel is adopted

$$\psi(x, L_c) = \frac{1}{2L_c} \exp\left(-\frac{|x|}{L_c}\right), \tag{74}$$

where $L_c = e_0 a_0$ is the length-scale parameter defining the nanostructure of the solid, e_0 is a material property, and a_0 represents an internal characteristic length. Many works on nonlocal structures have employed the kernel (74) proposed by Eringen (1983).

In the numerical applications presented in Section 6.2, the following two-dimensional kernel (Eringen, 1983) is adopted

$$\psi(x, y, L_c) = \frac{1}{\pi L_c^2} \exp\left(-\frac{x^2 + y^2}{L_c^2}\right). \tag{75}$$

The argument $(-x^2 - y^2)/L_c^2$ of the exponential function in Eq. (75) contains the Euclidean distance of the point (x, y), so that the kernel in Eq. (75) is invariant under coordinate transformation.

Table 15
Selective quadrature schemes adopted for the element stiffness matrices.

Element	Quadrature scheme	
	$\boldsymbol{K}_{\mathrm{b}}^{e}$	$\boldsymbol{K}_{\mathrm{s}}^{e}$
Q4	2×2	1×1
QL9	3×3	2×2
QL16	4×4	3×3
QGLL16	4×4	3×3

Appendix B. Shape functions of Lagrangian finite elements

In Section 6, standard Lagrangian finite elements are employed. Each two-dimensional element is defined by $n = m \times m$ nodes, where m denotes the number of nodes distributed along each side of the element.

The shape functions are defined in the parent coordinate system (ξ, η) over the bi-unit domain $[-1, 1] \times [-1, 1]$. The generic Lagrangian shape function associated with node a is expressed as

$$\hat{N}_a(\xi, \eta) = l_I(\xi)\, l_J(\eta) \qquad \begin{cases} a = m(J-1) + I, \\ I, J = 1, \dots, m, \end{cases} \tag{76}$$

where $l_I(\xi)$ and $l_J(\eta)$ are the one-dimensional Lagrange interpolation polynomials associated with the nodal coordinates ξ_I and η_J, respectively. They are given by

$$l_a(\xi) = \prod_{\substack{b=1 \\ b \neq a}}^{m} \frac{\xi - \xi_b}{\xi_a - \xi_b}, \quad \text{for} \quad a = 1, \dots, m. \tag{77}$$

The function $\hat{N}_a$ in Eq. (76) denotes the parent-domain representation of the physical shape function N_a introduced in Eq. (42). The specific Lagrangian finite elements adopted in Section 6 are summarized below.

- Q4: bi-linear quadrilateral element ($m = 2$), with nodal coordinates $\xi_1 = \eta_1 = -1$ and $\xi_2 = \eta_2 = 1$.
- QL9: bi-quadratic quadrilateral element ($m = 3$), with nodal coordinates $\xi_1 = \eta_1 = -1$, $\xi_2 = \eta_2 = 0$, and $\xi_3 = \eta_3 = 1$.
- QL16: bi-cubic quadrilateral element ($m = 4$), with equally spaced nodal coordinates $\xi_1 = \eta_1 = -1$, $\xi_2 = \eta_2 = -1/3$, $\xi_3 = \eta_3 = 1/3$, and $\xi_4 = \eta_4 = 1$.
- QGLL16: bi-cubic Gauss–Lobatto–Legendre quadrilateral element ($m = 4$), with nodal coordinates $\xi_1 = \eta_1 = -1$, $\xi_2 = \eta_2 = -1/\sqrt{5}$, $\xi_3 = \eta_3 = 1/\sqrt{5}$, and $\xi_4 = \eta_4 = 1$. This element features nodal clustering near the element vertices, which improves numerical accuracy for higher-order interpolations.

Unless otherwise stated, the selective quadrature reported in Table 15 is adopted for all the Lagrangian elements used in Section 6. Moreover, the higher-order quadrature employed for the evaluation of the bending stiffness matrix $\boldsymbol{K}_{\mathrm{b}}^{e}$ is consistently used to compute the nodal force contributions arising from the transverse load q and the inelastic curvature χ^{in} in Eq. (51), as well as to evaluate the nonlocal curvature χ^{nl} via the convolution integral in Eq. (57). Conversely, the lower-order quadrature adopted for the shear stiffness matrix $\boldsymbol{K}_{\mathrm{s}}^{e}$ is also used to compute the nodal forces associated with the inelastic shear strain $\gamma_{\mathrm{s}}^{\mathrm{in}}$ in Eq. (51) and to evaluate the nonlocal shear strain $\gamma_{\mathrm{s}}^{\mathrm{nl}}$ through the convolution integral in Eq. (57).

Reduced quadrature of the shear contribution may induce spurious mechanisms, namely nontrivial displacement fields $\tilde{\boldsymbol{u}} \neq \boldsymbol{0}$ satisfying

$$\boldsymbol{K}\tilde{\boldsymbol{u}} = \boldsymbol{0}, \tag{78}$$

where $\boldsymbol{K}$ denotes the assembled global stiffness matrix after imposition of the essential boundary conditions, so that rigid body modes are eliminated. When spurious mechanisms or other numerical anomalies (not observed in applications of Section 6) arise and compromise the solution, more robust finite elements (see, e.g., Oñate (2013) and Zienkiewicz et al. (2013)) may be adopted and incorporated into the iterative procedures proposed in this work for the analysis of nonlocal nanoplates.

Since possible spurious mechanisms may arise from selective quadrature, the tables in Section 6 also include results obtained with the bi-cubic element using full integration. These results are denoted by the acronym QL16-FI. For the 16-node elements, the results obtained using selective integration (QL16) and full integration (QL16-FI) are essentially identical. In this work, the acronyms Q4, QL9, QL16, and QGLL16 refer to finite elements employing the selective integration schemes reported in Table 15, whereas QL16-FI denotes the bi-cubic element with full 4×4 integration applied to all terms.

Data availability

Data will be made available on request.

References

Akgöz, B., & Civalek, O. (2011). Strain gradient elasticity and modified couple stress models for buckling analysis of axially loaded micro-scaled beams. *International Journal of Engineering Science*, *49*(11), 1268–1280.

Akgöz, B., & Civalek, Ö. (2022). Buckling analysis of functionally graded tapered microbeams via Rayleigh–Ritz method. *Mathematics*, *10*(23), http://dx.doi.org/10.3390/math10234429.

Alotta, G., Russillo, A. F., & Failla, G. (2025). Elastic wave propagation in periodic stress-driven nonlocal Timoshenko beams. *International Journal of Solids and Structures*, *306*, Article 113103. http://dx.doi.org/10.1016/j.ijsolstr.2024.113103.

Ansari, R., & Gholami, R. (2016). Nonlocal free vibration in the pre- and post-buckled states of magneto-electro-thermo elastic rectangular nanoplates with various edge conditions. *Smart Materials and Structures*, *25*(9), http://dx.doi.org/10.1088/0964-1726/25/9/095033.

Ansari, R., Torabi, J., & Norouzzadeh, A. (2018). Bending analysis of embedded nanoplates based on the integral formulation of Eringen's nonlocal theory using the finite element method. *Physica B. Condensed Matter*, *534*, 90–97. http://dx.doi.org/10.1016/j.physb.2018.01.025.

Barchiesi, E., dell'Isola, F., & Hild, F. (2021). On the validation of homogenized modeling for bi-pantographic metamaterials via digital image correlation. *International Journal of Solids and Structures*, *208–209*, 49–62. http://dx.doi.org/10.1016/j.ijsolstr.2020.09.036.

Barretta, R., Čanađija, M., Luciano, R., & Marotti de Sciarra, F. (2022). On the mechanics of nanobeams on nano-foundations. *International Journal of Engineering Science*, *180*, Article 103747. http://dx.doi.org/10.1016/j.ijengsci.2022.103747.

Barretta, R., Caporale, A., Faghidian, S. A., Luciano, R., Marotti de Sciarra, F., & Medaglia, C. M. (2019). A stress-driven local-nonlocal mixture model for Timoshenko nano-beams. *Composites Part B: Engineering*, *164*, 590–598. http://dx.doi.org/10.1016/j.compositesb.2019.01.012.

Barretta, R., Faghidian, S. A., & Marotti de Sciarra, F. (2019). Stress-driven nonlocal integral elasticity for axisymmetric nano-plates. *International Journal of Engineering Science*, *136*, 38–52. http://dx.doi.org/10.1016/j.ijengsci.2019.01.003.

Barretta, R., Luciano, R., Marotti de Sciarra, F., & Vaccaro, M. S. (2024). Modelling issues and advances in nonlocal beams mechanics. *International Journal of Engineering Science*, *198*, http://dx.doi.org/10.1016/j.ijengsci.2024.104042.

Barretta, R., & Marotti de Sciarra, F. (2019). Variational nonlocal gradient elasticity for nano-beams. *International Journal of Engineering Science*, *143*, 73–91. http://dx.doi.org/10.1016/j.ijengsci.2019.06.016.

Barretta, R., Marotti de Sciarra, F., & Vaccaro, M. S. (2023). Nonlocal elasticity for nanostructures: A review of recent achievements. *Encyclopedia*, *3*(1), 279–310. http://dx.doi.org/10.3390/encyclopedia3010018.

Batool, F., Muhammad, S., Muazzam, R., Waqas, M., Ullah, Z., Roy, S., Zhang, Y., Wang, K., & Guo, B. (2025). Advancements in graphene-based composites: A review of the emerging applications in healthcare. *Smart Materials in Medicine*, *6*(1), 120–138. http://dx.doi.org/10.1016/j.smaim.2025.01.001.

Behnam-Rasouli, M.-S., Challamel, N., Karamodin, A., & Sani, A. A. (2024). Application of the Green's function method for static analysis of nonlocal stress-driven and strain gradient elastic nanobeams. *International Journal of Solids and Structures*, *295*, Article 112794. http://dx.doi.org/10.1016/j.ijsolstr.2024.112794.

Caporale, A., Darban, H., & Luciano, R. (2022). Nonlocal strain and stress gradient elasticity of Timoshenko nano-beams with loading discontinuities. *International Journal of Engineering Science*, *173*, http://dx.doi.org/10.1016/j.ijengsci.2021.103620.

Caporale, A., Luciano, R., Scorza, D., & Vantadori, S. (2023). Local–nonlocal stress-driven model for multi-cracked nanobeams. *International Journal of Solids and Structures*, *273*, Article 112230. http://dx.doi.org/10.1016/j.ijsolstr.2023.112230.

Caporale, A., Vaccaro, M. S., Barretta, R., & Luciano, R. (2025). Nonlocal elastic plate problems via iterative method. *Mechanics Research Communications*, *150*, Article 104538. http://dx.doi.org/10.1016/j.mechrescom.2025.104538.

Challamel, N., & Wang, C. M. (2008). The small length scale effect for a non-local cantilever beam: A paradox solved. *Nanotechnology*, *19*(34), http://dx.doi.org/10.1088/0957-4484/19/34/345703.

Darban, H., Luciano, R., Caporale, A., & Basista, M. (2022). Modeling of buckling of nanobeams embedded in elastic medium by local-nonlocal stress-driven gradient elasticity theory. *Composite Structures*, *297*, http://dx.doi.org/10.1016/j.compstruct.2022.115907, Cited by: 0.

Ding, W., & Semperlotti, F. (2024). A multimesh finite element method for integral nonlocal elasticity using mesh-decoupling technique. *International Journal of Mechanical Sciences*, *275*, Article 109260. http://dx.doi.org/10.1016/j.ijmecsci.2024.109260.

Eringen, A. (1972). Linear theory of nonlocal elasticity and dispersion of plane waves. *International Journal of Engineering Science*, *10*(5), 425–435.

Eringen, A. C. (1983). On differential equations of nonlocal elasticity and solutions of screw dislocation and surface waves. *Journal of Applied Physics*, *54*(9), 4703–4710. http://dx.doi.org/10.1063/1.332803.

Eringen, A. (1992). Vistas of nonlocal continuum physics. *International Journal of Engineering Science*, *30*(10), 1551–1565.

Fallahzadeh Rastehkenari, S., Dargahi, J., & Packirisamy, M. (2026). Random vibrations of two phase shear deformable pieozoelectric nanobeams based on Gaussian local/nonlocal integral model. *Probabilistic Engineering Mechanics*, *83*, Article 103899. http://dx.doi.org/10.1016/j.probengmech.2026.103899.

Farajpour, A., Howard, C. Q., & Robertson, W. S. (2020). On size-dependent mechanics of nanoplates. *International Journal of Engineering Science*, *156*, http://dx.doi.org/10.1016/j.ijengsci.2020.103368.

Farooq, S. A., Raina, A., Mohan, S., Singh, R. A., Jayalakshmi, S., & Haq, M. I. U. (2022). Nanostructured coatings: Review on processing techniques, corrosion behaviour and tribological performance. *Nanomaterials*, *12*(8), http://dx.doi.org/10.3390/nano12081323.

Fernández-Sáez, J., & Zaera, R. (2017). Vibrations of Bernoulli-Euler beams using the two-phase nonlocal elasticity theory. *International Journal of Engineering Science*, *119*, 232–248. http://dx.doi.org/10.1016/j.ijengsci.2017.06.021.

Fleck, N., & Hutchinson, J. (1997). In J. W. Hutchinson, & T. Y. Wu (Eds.), *Advances in applied mechanics*: *vol. 33*, *Strain gradient plasticity* (pp. 295–361). Elsevier, http://dx.doi.org/10.1016/S0065-2156(08)70388-0.

Grekov, M., & Bochkarev, A. (2024). Buckling of a stretched nanoplate with a nanohole incorporating surface energy. *International Journal of Engineering Science*, *199*, http://dx.doi.org/10.1016/j.ijengsci.2024.104075.

He, D., Li, W., Vaziri, V., & Aphale, S. S. (2024). Thermo-electro-mechanical vibration analysis for piezoelectric plates under two-parameter elastic foundation with general boundary conditions. *International Journal of Engineering Science*, *201*, http://dx.doi.org/10.1016/j.ijengsci.2024.104057.

Hu, Y., Yu, Y., & Madenci, E. (2020). Peridynamic modeling of composite laminates with material coupling and transverse shear deformation. *Composite Structures*, *253*, http://dx.doi.org/10.1016/j.compstruct.2020.112760.

Izadi, R., Das, R., Fantuzzi, N., & Trovalusci, P. (2024). Fracture properties of green nano fibrous network with random and aligned fiber distribution: A hierarchical molecular dynamics and peridynamics approach. *International Journal of Engineering Science*, *204*, Article 104136. http://dx.doi.org/10.1016/j.ijengsci.2024.104136.

Jafarinezhad, M., Sburlati, R., & Cianci, R. (2023). Static and free vibration analysis of functionally graded annular plates using stress-driven nonlocal theory. *European Journal of Mechanics. A. Solids*, *99*, http://dx.doi.org/10.1016/j.euromechsol.2023.104955.

Jafarinezhad, M., Sburlati, R., & Cianci, R. (2024). Nonlocal stress-driven model for functionally graded Mindlin annular plate: bending and vibration analysis. *Archive of Applied Mechanics*, *94*(5), 1313–1333. http://dx.doi.org/10.1007/s00419-024-02577-7.

Karami, B., & Ghayesh, M. H. (2025). Elastic waves in graphene origami-enabled auxetic metamaterial thickness-deformable doubly-curved shells. *International Journal of Engineering Science*, *211*, http://dx.doi.org/10.1016/j.ijengsci.2025.104249.

Ke, L.-L., Yang, J., Kitipornchai, S., & Wang, Y.-S. (2014). Axisymmetric postbuckling analysis of size-dependent functionally graded annular microplates using the physical neutral plane. *International Journal of Engineering Science*, *81*, 66–81. http://dx.doi.org/10.1016/j.ijengsci.2014.04.005.

Khaniki, H. B. (2019). On vibrations of FG nanobeams. *International Journal of Engineering Science*, *135*, 23–36. http://dx.doi.org/10.1016/j.ijengsci.2018.11.002.

Kröner, E. (1967). Elasticity theory of materials with long range cohesive forces. *International Journal of Solids and Structures*, *3*(5), 731–742. http://dx.doi.org/10.1016/0020-7683(67)90049-2.
Lam, D., Yang, F., Chong, A., Wang, J., & Tong, P. (2003). Experiments and theory in strain gradient elasticity. *Journal of the Mechanics and Physics of Solids*, *51*(8), 1477–1508. http://dx.doi.org/10.1016/S0022-5096(03)00053-X.
Li, H., & Vlassak, J. J. (2009). Determining the elastic modulus and hardness of an ultra-thin film on a substrate using nanoindentation. *Journal of Materials Research*, *24*(3), 1114–1126. http://dx.doi.org/10.1557/jmr.2009.0144.
Li, G., Xing, Y., & Wang, Z. (2021). Closed-form solutions for free vibration of rectangular nonlocal Mindlin plates with arbitrary homogeneous boundary conditions. *Composites Part C: Open Access*, *6*, Article 100193. http://dx.doi.org/10.1016/j.jcomc.2021.100193.
Li, H., Yao, L., Li, C., & Guo, L. (2025). Capturing the nonlocal effect using a novel hybrid 8-node plate element based on the Hellinger–Reissner variational principle. *Engineering with Computers*, *41*(2), 1011–1035. http://dx.doi.org/10.1007/s00366-024-02061-4.
Liu, S., Shen, Y., Li, Y., Mo, Y., Yu, E., Ge, T., Li, P., & Li, J. (2026). Dynamic network- and microcellular architecture-driven biomass elastomer toward sustainable and versatile soft electronics. *Nano-Micro Letters*, *18*(1), http://dx.doi.org/10.1007/s40820-025-01942-7.
Lovisi, G., Feo, L., Lambiase, A., & Penna, R. (2024). Application of surface stress-driven model for higher vibration modes of functionally graded nanobeams. *Nanomaterials*, *14*(4), http://dx.doi.org/10.3390/nano14040350.
Lu, L., Guo, X., & Zhao, J. (2018). On the mechanics of Kirchhoff and Mindlin plates incorporating surface energy. *International Journal of Engineering Science*, *124*, 24–40.
Lu, L., Guo, X., & Zhao, J. (2019). A unified size-dependent plate model based on nonlocal strain gradient theory including surface effects. *Applied Mathematical Modelling*, *68*, 583–602. http://dx.doi.org/10.1016/j.apm.2018.11.023.
Maugin, G. A. (2017). *Non-classical continuum mechanics - A dictionary*. Singapore: Springer.
Meyers, M., Mishra, A., & Benson, D. (2006). Mechanical properties of nanocrystalline materials. *Progress in Materials Science*, *51*(4), 427–556. http://dx.doi.org/10.1016/j.pmatsci.2005.08.003.
Nateghi-Babagi, P., Navayi-Neya, B., & Eskandari-Ghadi, M. (2025). Free vibration and buckling analysis of simply supported rectangular nano-plates: A closed-form solution based on nonlocal 3D elasticity theory. *International Journal of Solids and Structures*, *312*, Article 113261. http://dx.doi.org/10.1016/j.ijsolstr.2025.113261.
Nazmul, I., & Devnath, I. (2021). Closed-form expressions for bending and buckling of functionally graded nanobeams by the Laplace transform. *International Journal of Computational Materials Science and Engineering*, http://dx.doi.org/10.1142/S2047684121500123.
Nguyen, H., Challamel, N., & Wang, C. (2025). Analytical solutions for free vibrations of rectangular cuboid elastic lattices and their continuous approximations. *Journal of Sound and Vibration*, *600*, Article 118836. http://dx.doi.org/10.1016/j.jsv.2024.118836.
Nguyen-Tri, P., Nguyen, T. A., Carriere, P., & Ngo Xuan, C. (2018). Nanocomposite coatings: Preparation, characterization, properties, and applications. *International Journal of Corrosion*, *2018*, http://dx.doi.org/10.1155/2018/4749501.
Numanoğlu, H. M., Ersoy, H., Akgöz, B., & Civalek, Ö. (2022). A new eigenvalue problem solver for thermo-mechanical vibration of Timoshenko nanobeams by an innovative nonlocal finite element method. *Mathematical Methods in the Applied Sciences*, *45*(5), 2592–2614. http://dx.doi.org/10.1002/mma.7942.
Oñate, E. (2013). *Structural analysis with the finite element method - Linear statics* (pp. 1–863).
Peddieson, J., Buchanan, G., & McNitt, R. (2003). Application of nonlocal continuum models to nanotechnology. *International Journal of Engineering Science*, *41*(3–5), 305–312.
Penna, R., & Lovisi, G. (2025). Surface and nonlocal effects in piezoelectric nanobeams. *European Journal of Mechanics. A. Solids*, *113*, Article 105715. http://dx.doi.org/10.1016/j.euromechsol.2025.105715.
Reddy, J. (2010). Nonlocal nonlinear formulations for bending of classical and shear deformation theories of beams and plates. *International Journal of Engineering Science*, *48*(11), 1507–1518.
Rezaei, A., Izadi, R., & Fantuzzi, N. (2025). A non-classical computational method for modelling functionally graded porous planar media using micropolar theory. *Computers and Structures*, *306*, Article 107590. http://dx.doi.org/10.1016/j.compstruc.2024.107590.
Romano, G., & Barretta, R. (2017). Nonlocal elasticity in nanobeams: the stress-driven integral model. *International Journal of Engineering Science*, *115*, 14–27.
Romano, G., Barretta, R., & Diaco, M. (2019). Iterative methods for nonlocal elasticity problems. *Continuum Mechanics and Thermodynamics*, *31*(3), 669–689. http://dx.doi.org/10.1007/s00161-018-0717-8.
Romano, G., Barretta, R., Diaco, M., & Marotti de Sciarra, F. (2017). Constitutive boundary conditions and paradoxes in nonlocal elastic nanobeams. *International Journal of Mechanical Sciences*, *121*, 151–156.
Romano, G., Luciano, R., Barretta, R., & Diaco, M. (2018). Nonlocal integral elasticity in nanostructures, mixtures, boundary effects and limit behaviours. *Continuum Mechanics and Thermodynamics*, *30*(3), 641–655.
Sadeghian, M., Palevicius, A., Griskevicius, P., & Janusas, G. (2024). Nonlinear analysis of the multi-layered nanoplates. *Mathematics*, *12*(22), http://dx.doi.org/10.3390/math12223545.
Saha, R., & Nix, W. D. (2002). Effects of the substrate on the determination of thin film mechanical properties by nanoindentation. *Acta Materialia*, *50*(1), 23–38. http://dx.doi.org/10.1016/S1359-6454(01)00328-7.
Saini, R., & Pradyumna, S. (2023). Asymmetric vibrations of functionally graded annular nanoplates under thermal environment using nonlocal elasticity theory with modified nonlocal boundary conditions. *Journal of Engineering Mechanics*, *149*(5), http://dx.doi.org/10.1061/JENMDT.EMENG-7016.
Shaat, M. (2015). Iterative nonlocal elasticity for Kirchhoff plates. *International Journal of Mechanical Sciences*, *90*, 162–170. http://dx.doi.org/10.1016/j.ijmecsci.2014.11.004.
Vaccaro, M. S., & Sedighi, H. M. (2023). Two-phase elastic axisymmetric nanoplates. *Engineering with Computers*, *39*(1), 827–834. http://dx.doi.org/10.1007/s00366-022-01680-z.
Voevodin, A., & Zabinski, J. (2005). Nanocomposite and nanostructured tribological materials for space applications. *Composites Science and Technology*, *65*(5), 741–748. http://dx.doi.org/10.1016/j.compscitech.2004.10.008.
Wang, Q., & Liew, K. (2007). Application of nonlocal continuum mechanics to static analysis of micro- and nano-structures. *Physics Letters, Section A: General, Atomic and Solid State Physics*, *363*(3), 236–242.
Wang, X., Yu, J., Zhang, B., Elmaimouni, L., & Li, L. (2025). Lamb waves in piezoelectric quasicrystal multi-layered nano-plates with imperfect interfaces. *Composite Structures*, *370*, http://dx.doi.org/10.1016/j.compstruct.2025.119430.
Xiao, M., Xu, A., Sui, Z., Zhang, W., Liu, H., & Lee, C. (2025). Multifunctional MEMS, NEMS, micro/nano-structures enabled by piezoelectric and ferroelectric effects. *Nanoscale Horizons*, http://dx.doi.org/10.1039/d5nh00386e.
Xie, P., Chi, C., Yang, Y., Hong, F., Hao, H., & Yan, S. (2025). SnO2 nanoplates via structural modulation enabling selective and sensitive NO2 detection at ppb level. *Sensors and Actuators B: Chemical*, *442*, http://dx.doi.org/10.1016/j.snb.2025.138125.
Xu, X.-J., & Wang, B. (2025). On size-dependent mechanics of Mindlin plates made of polymer networks. *International Journal of Engineering Science*, *206*, http://dx.doi.org/10.1016/j.ijengsci.2024.104164.
Yang, C., Yu, J., Liu, C., Zhang, B., & Elmaimouni, L. (2026). The applicability of nonlocal shear deformation theory and scale parameters for guided wave propagation in nanoplates. *European Journal of Mechanics. A. Solids*, *116*, Article 105872. http://dx.doi.org/10.1016/j.euromechsol.2025.105872.
Zhang, H., Yu, L., Li, R., Zhao, F., Guo, L., Wang, P.-h., Cao, W., Ding, Z.-j., & Qiao, Z. (2024). Layer-tunable synthesis of tetragonal Pr-doped SnO2 nanoplates for enhanced sensitive SO2 sensor. *Sensors and Actuators B: Chemical*, *409*, http://dx.doi.org/10.1016/j.snb.2024.135629.
Zhou, S., Qi, L., Zhang, R., Li, A., Ren, F., Zheng, Z., Qiao, J., Sun, Y., & Zhou, S. (2025). Analysis of the electromechanical responses of sandwich circular nano-plate based on flexoelectric nano-ultrasonic transducer. *Applied Mathematical Modelling*, *137*, http://dx.doi.org/10.1016/j.apm.2024.115697.
Zienkiewicz, O., Taylor, R., & Zhu, J. (2013). *The finite element method: Its basis and fundamentals: Seventh edition* (pp. 1–714). http://dx.doi.org/10.1016/C2009-0-24909-9.